

# Plasma points and radiative collapse in vacuum sparks

K. N. Koshelev

*Institute for Spectroscopy, USSR Academy of Sciences, 142092 Troitsk, USSR*

N. R. Pereira

*Berkeley Research Associates, P. O. Box 852, Springfield, Virginia 22150*

(Received 2 April 1990; accepted for publication 5 February 1991)

This review discusses the intense x-ray emitting regions, called plasma points, that appear in low-inductance vacuum sparks and other high-current discharges. Accurate x-ray spectroscopy indicates the existence of two types of plasma points with different plasma parameters. One type is extremely small ( $\sim$ microns), dense ( $\sim 10^{23}/\text{cm}^3$ ), and hot ( $\geq 1$  keV), while the second type is an order of magnitude less extreme. A dynamic model (Vikhrev 1982a) based on radiation cooling with axial outflow of plasma predicts a radiative collapse that is consistent with many features of the plasma points.

## I. INTRODUCTION

The high voltage vacuum discharge was proposed more than 70 years ago as a spectroscopic source (Millikan 1918). The original apparatus operated at high voltage with a relatively modest current, typically 100 kV and less than 100 kA. In the mid-sixties (Cohen 1968) the power of the trigger electrode was increased, the inductance was reduced to less than about 100 nH and the voltage to  $\sim 20$ –50 kV, while the capacitance was increased to  $\sim 10$ –20  $\mu\text{F}$ . The resulting apparatus is the “low-inductance vacuum spark.”

The peak current in the low-inductance vacuum spark is more than 100 kA, and the trigger injects a significant amount of material in the interelectrode vacuum. Both the higher current and the presence of material between the electrodes are needed to make the low-inductance vacuum spark into an intense source of x-rays from highly ionized ions. The low-inductance vacuum spark is now a widely used research tool and an intensively studied research object. The discharge has many interesting features that are easily observed qualitatively but were unanticipated theoretically, e.g., pulsed x rays, multiply ionized atoms, and electron and ion beams.

It is relatively easy to produce hot, highly ionized plasma despite the low-inductance vacuum spark's modest energy ( $\sim 3$ –30 kJ). Already the first experiments (Cohen 1968) measured spectra of He- and H-like ions of titanium and iron (Ti XXI–XXII; Fe XXV–XXVI); somewhat later (Beier 1978) observed the resonance transition of the He-like ion Mo XLI ( $\lambda = 0.69 \text{ \AA}$ ). In pinhole photographs the K-line radiation appears to come from small, pointlike regions in the plasma that are called plasma points, bright spots, or hot spots. The relative simplicity and high shot rate of the low-inductance vacuum spark allow a thorough study of the formation dynamics of the plasma point and the properties of its plasma.

This review describes experimental investigations of the plasma point in low-inductance vacuum sparks. In addition, the review interprets many aspects of the plasma points with the radiative collapse model (Vikhrev 1982a; Koshelev 1985). The literature contains alternate models

that we mention but do not discuss because, in our opinion, they are not far enough developed for comparison to experiment. Likewise, we do not discuss in detail the bright spots that occur in more powerful discharges because their analysis emphasizes bulk x-ray production by implosion (Pereira 1988b). However, plasma points and bright spots appear to be related, and insight in plasma points could become useful in understanding bright spots.

It should be emphasized that the plasma point is by its very nature a dynamic phenomenon with constantly changing parameters. For example, during its development the temperature of the plasma point changes from tens of electron volts to several kilovolts. The size and density of the plasma point also change significantly, e.g., from 1 mm to less than 10  $\mu\text{m}$  and from  $10^{19}/\text{cm}^3$  to  $10^{23}/\text{cm}^3$ . Moreover, the plasma point must have spatial gradients in temperature and density that cannot always be resolved experimentally. Therefore it is necessary to keep in mind that a particular measurement may apply only to a specific phase in the development of the plasma point. This realization may help eliminate disparities between experimental results, resulting in an improved description of the plasma point.

A previous review (Korop 1979) summarizes the first ten years of research on the low-inductance vacuum spark. The devices used in various laboratories (e.g., Cilliers 1975; Turechek 1975; Golts 1975; Kononov 1977; Veretenikov 1981; Negus 1979; Morita 1983) have capacitances of 10–30  $\mu\text{F}$  charged to 10–20 kV, with a circuit inductance of 50–100 nH. The discharge current is typically a damped sinusoid with peak amplitude  $I_m \approx 150$ –200 kA and pulse length  $\approx 1.5$ –2  $\mu\text{s}$ . The discharge is ignited by an electrical trigger in the cathode or by irradiating the anode with a powerful laser (Lee 1974; Koloshnikov 1985).

With an electrical trigger the initial stage of the discharge is characterized by an erratic initial current and an x-ray pulse from the anode, and by the formation of plasma jets from the electrodes (e.g., Epstein 1970). The trigger pulse forms the cathode plasma: the anode plasma is produced by bombardment of the anode surface by a beam of electrons from the cathode plasma accelerated in the electric field between the electrodes. The anode and cathode

plasmas move toward each other with velocities  $\approx 10^6$  cm/s. The initial phase is complete when plasma bridges the vacuum gap: the voltage across the gap  $V_g$  drops to  $V_g \approx L_g dI/dt$  ( $L_g$  is the inductance of the current channel).

In the next phase of the discharge the current increases as prescribed by the circuit voltage  $V$  and inductance  $L$  of the circuit,  $dI/dt = V/L$ . On top of the smoothly rising current there appear short ( $< 100$  ns) single or multiple dips in the current. These current dips are accompanied by intense bursts of x rays. The dips have a random character, although many authors have noted that they depend on discharge initiation, circuit parameters, and the material and shape of the electrodes (e.g., Cilliers 1975; Negus 1979).

The current dips are correlated with the appearance of plasma points. The plasma point principally emits x-ray lines from ions of the anode material; radiation from cathode material is weak. However, the trigger to the cathode must be sufficiently strong for a plasma point to develop (Sidel'nikov 1982a).

Triggering the low-inductance vacuum spark by irradiating the anode with a laser produces the anode jet directly. The erratic initial current is now absent, and the current starts slightly after the laser pulse. After this initial stage the discharge develops as described above (Koloshnikov 1985).

The x-ray pulses correlated with the dips in the current and the formation of plasma points contain photons with a wide range of energies, typically  $h\nu \approx 5$ –150 keV (e.g., Cohen 1968; Lee 1974; Cilliers 1975; Veretennikov 1981). The x-ray spectrum contains information about the plasma in the plasma point. The name "plasma point" is particularly apt when looking at photons with  $h\nu < 10$  keV, corresponding to resonance transitions in He- and H-like ionization states of moderately heavy ions (nuclear charge  $Z_n < 30$ ); the points are often less than  $10 \mu\text{m}$  in size.

Higher energy photons may appear to be less localized. Typically, the x-ray spectrum below  $h\nu \sim 150$  keV is emitted from a plasma with electron temperature  $T_e \sim 10$  keV. For the relatively few photons with  $h\nu > 150$  keV the spectrum decreases with photon energy according to a power law (Cilliers 1975; Fukai 1975). Some discharges show even more energetic quanta with energies  $h\nu > 500$  keV (Lee 1974).

This review is principally concerned with the two types of plasma points (Aglitskii 1986; Antsiferov 1989) that appear in low-inductance vacuum sparks. The first type consists of a minute region of ions stripped to the  $K$ -shell, with size around  $\sim 10 \mu\text{m}$  or less as shown below in Fig. 1. According to the radiative collapse theory a type-1 plasma point is a short stage in the radiative collapse of a pinch: the collapse process is called micropinching, and a type-1 plasma point is sometimes called a micropinch. A type-2 plasma point is an order of magnitude larger and radiates few (or no) resonance lines: its radiation is insufficient for a full collapse, and is sometimes referred to as a hot (or bright) spot.

Not all localized regions of intense x-ray emission in

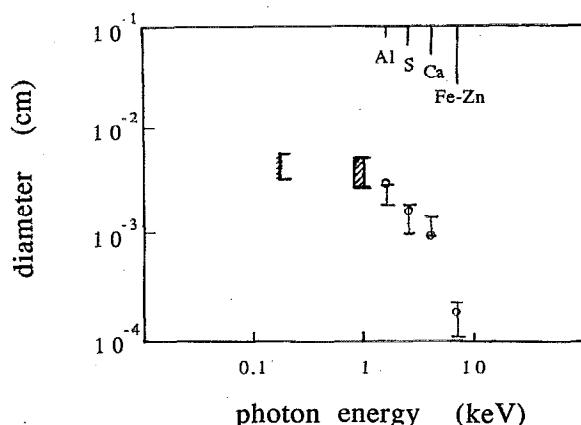


FIG. 1. Plasma point size vs photon energy  $1 < h\nu < 10$  keV of the resonance line (the corresponding element is on top). The bracket is the size of an iron plasma point measured with softer photons exceeding 1 keV, the line around 0.1 keV is the size seen with softer photons.

other types of vacuum sparks or other pulse power devices can be classified in these two categories. For example, some generators of short electrical pulses used in exploding wire research have a sizable prepulse. The prepulse could result in a hollow cylinder of plasma surrounding the wire (e.g., Aranchuk 1986), and develop into striations that radiate x rays. These structures fall outside the present review.

Intense soft x-ray emission from small regions is also common in radiative z-pinch discharges on relativistic electron beam generators (Pereira 1988b). These z-pinches differ from vacuum sparks in their higher currents ( $\sim 1$  MA) and shorter pulse times ( $\sim 100$  ns); moreover, z-pinches have ample material between the electrodes before the start of the electrical pulse. In the context of z pinches these regions are called "bright spots" (or sometimes hot spots): their diameter is quoted as  $50$ – $100 \mu\text{m}$  (Stallings 1979; Burkhalter 1979; Riordan 1981). Compared to the extremely high electron densities ( $n_e \sim 10^{23}/\text{cm}^3$ ) in low-inductance vacuum sparks, the x-ray spectra in z pinches indicate much lower electron densities, even in the bright spots ( $n_e \sim 10^{21}$ : e.g., Deeney 1989). Perhaps these lower values reflect the spectral features used in the interpretation. However, when a single group looks at both vacuum sparks and z pinches the bright spots in z pinches seem identical to plasma points (Alikhanov 1984; Gol'ts 1986; Gol'ts 1987). They document a 1-MA discharge through a gas puff in Kr ( $Z_n = 36$ ) and Xe ( $Z_n = 54$ ), with plasma points of  $\approx 5 \mu\text{m}$  diameter in He-like Kr and Xe. At this time we believe that bright spots in z pinches are similar to plasma points in vacuum sparks, at least in part (e.g., Sopykin 1990). The same is true for the bright spots seen in the plasma focus, but this device, used mostly for thermonuclear fusion research, falls outside this review.

## II. THE PLASMA POINT: EXPERIMENTAL DATA

This section describes the experimental results on the formation of the plasma points, their size, and the plasma parameters temperature and density. In the older literature these parameters have a confusingly large range of values.

One reason is the existence of two types of plasma points. Another reason is that plasma points are dynamic entities, wherein the plasma parameters change rapidly over a large range of values. Plasma thermometry or densitometry applies to a limited range of plasma parameters, and therefore each measurement method gives a value characteristic of the method's range of applicability. Section III below describes the radiative collapse model that gives a coherent description of plasma points.

### A. Plasma point size

Already the first investigators of low-inductance vacuum sparks noted that very small regions in the plasma produce the bulk of the x rays. In pinhole pictures these regions show up as bright spots or points, whence their name plasma points. The plasma points are elongated: for example, in discharges of titanium and iron the size of the plasma point perpendicular to the discharge axis was estimated as  $<3\text{--}4\ \mu\text{m}$  (Schwob 1972; Klapisch 1977), or  $<10\ \mu\text{m}$  (Morita 1983; Veretennikov 1985) to  $20\text{--}50\ \mu\text{m}$  (Lee 1975). Along the pinch axis the size is 3–10 times larger. These size measurements are typically carried out with pinhole cameras with filters that pass the resonance and characteristic lines of the respective elements (and the few available higher-energy photons). These measurements will be called "K measurements," because most photons originate in the K-shell of the element.

It became clear later that there are two types of K measurements. The first type of K measurement looks at the resonance lines, and characterizes the plasma point in the stage wherein the plasma consists of ions stripped to the K shell. The second type of K measurements sees characteristic lines of low-multiplicity ions. These lines are probably excited by suprathreshold electrons or electron beams in a much cooler plasma.

The two types of K measurements define two types of plasma points: the plasma points of the first type are an order of magnitude smaller than the plasma points of the second type. Much confusion in published measurements was clarified by the recognition of these two types of plasma points (Aglitskii 1986; Antsiferov 1989; and below). For a wide range of elements they measure the K size of the plasma point from its magnified image through a square pinhole. The blurring of the edge determines the length and width of the plasma point even when the pinhole is relatively large.

A pinhole image gives an overestimate of the plasma size. When the pinhole is small compared to the x-ray source the source size is the size of the image divided by the magnification, but when the pinhole is large compared to the source the image reflects the size of the pinhole irrespective of the dimensions of the source: a point source still produces an extended image. However, a point source gives an image with sharp edges, while the image is blurred with an extended source. The width of the blurring is the magnification times the source size if the effects from diffraction and film grain size are suppressed.

Fresnel diffraction smears out the image over a distance  $\delta_f \sim \sqrt{\lambda R}$ , where  $\lambda$  is the x-ray wavelength and  $R$

is the distance between plasma point and the pinhole. For iron with  $\lambda \sim 0.2\ \text{nm}$  and a typical distance  $R \approx 2\ \text{cm}$  the Fresnel diffraction gives a contribution of  $\approx 2\ \mu\text{m}$ . The contribution from film grain size can be suppressed by using sufficient magnification: the grains are  $\sim 10\ \mu\text{m}$ , and their influence is reduced to below  $2\ \mu\text{m}$  when the magnification exceeds  $\sim 5$ . The total effect from Fresnel diffraction and grain size is therefore less than  $\sim 2\ \mu\text{m}$ . In addition, any motion of the source smears out the image and adds to the blurring of the edge, but this does not seem to be a problem (see below).

The plasma point size was measured carefully (Antsiferov 1989) in the resonance lines of He- and H-like iron, with  $5\times$  magnification. Fresnel diffraction is eliminated by putting the pinhole close to the source,  $1 < R < 5$ . Parallel and perpendicular sizes are measured simultaneously by orienting the square pinhole along the axis of the discharge. The plasma point blurred the edge of the image less than  $15\text{--}20\ \mu\text{m}$  perpendicular to the axis and  $25\text{--}50\ \mu\text{m}$  along the axis. Thus, the perpendicular size  $d$  of the plasma point for this iron plasma is  $d < 2\ \mu\text{m}$ , and the aspect ratio  $\alpha \sim 3\text{--}5$ . Analogous measurements carried out for plasmas of aluminum ( $Z_n = 13$ ) give  $d \sim 20\text{--}30\ \mu\text{m}$ , for a plasma of sulfur ( $Z_n = 16$ ) and calcium ( $Z_n = 20$ )  $d \sim 10\text{--}15\ \mu\text{m}$ , and  $d < 2\ \mu\text{m}$  for all heavier elements (Fe,  $Z_n = 26$ ; Cu,  $Z_n = 29$ ; Zn,  $Z_n = 30$ ). The four right-most points in Fig. 1 give these K measurements for the size of the plasma point with the different elements as indicated.

The filter in front of the pinhole can be chosen to transmit the x rays from the L shell of moderately heavy elements, i.e., photons with  $h\nu \sim 1\ \text{keV}$ . The plasma point seen in this light is larger than indicated by the K measurements. For example, the perpendicular size of the plasma point in the L shell light for an iron pinch (Veretennikov 1985) is  $\sim 30\ \mu\text{m}$ , and the aspect ratio is  $\sim 3\text{--}5$ . Figure 1 gives this point by the rectangle around  $h\nu \sim 1\ \text{keV}$ .

Churilov *et al.* (1990) measured the plasma points size for iron in a broad range of the VUV spectrum, from 5 nm (0.25 keV) to 20 nm (0.08 keV), using a spatially resolved VUV spectrum from a grazing incidence spectrograph. Spatial resolution in the direction perpendicular to the discharge axis is possible with an additional slit. The blur in the edge of the spectrum allows the determination of the effective size of the source of emission for each of the wavelengths separately, similar to the size measurement with a square pinhole. The left-top line in Fig. 1 gives the results. The size of the iron plasma point decreases with wavelength, from  $420\text{--}450\ \mu\text{m}$  for  $\lambda = 20\ \text{nm}$  to about  $300\ \mu\text{m}$  for  $\lambda = 5\ \text{nm}$ .

The existence of certain x-ray lines gives a rough indication of the plasma temperature. Therefore it is possible to correlate plasma point size with plasma temperature. How to determine the plasma point temperature is discussed in the next subsection.

### B. Plasma point temperature

A stationary blob of plasma with uniform temperature, density, and size emits a complicated spectrum that is fully

characterized by these three parameters. In principle, only three spectral features suffice to determine the three parameters. The remainder of the spectrum can serve as a consistency check. However, determining the parameters for a real plasma point from a measured spectrum gives different values depending on which part of the spectrum is used.

Obvious reasons for this discrepancy are spatial gradients and time dependence. Spatial gradients are unavoidable when hot plasma is sitting in colder surroundings. Unfolding gradients from spectra measured along a line of sight is difficult, and therefore rarely done (Gersten 1986) despite the importance of gradients in virtually all plasma points.

In a plasma point the temperature changes over one or two orders of magnitude in such a short time ( $\sim 30$  ps) that only time-integrated spectra have been taken up to now. The time-integrated spectrum contains the signature of the various stages in the plasma point evolution. Each stage contributes principally to a specific spectral region, but with substantial overlap between the regions. Measurements of the plasma parameters could differ substantially, depending on the spectral region used for the measurement.

Additional problems arise if the plasma is not in ionization equilibrium as it heats up or cools down. Ionization equilibrium can only be obtained if the plasma goes through each ionization stage slowly, staying longer than a time  $\tau$  that depends on the electron density, the element, and its ionization state (Kononov 1977, and below). For example, for a Ne-like iron plasma to reach the He-like ionization state  $n_e\tau$  must exceed  $10^{11}$  cm<sup>3</sup>/s. Sometimes a beam of electrons creates additional radiation. Given these complexities extreme caution is needed in unfolding experimentally measured spectra from plasma points (or any plasma). Much confusion in the published values of plasma parameters is due to insufficient appreciation of the complicated nature of plasma point spectra.

Consider the plasma point temperature. In the first experiments an electron temperature  $T_e \gg 1$ –2 keV was inferred from the K-line spectra of iron and titanium. On the other hand, measurement of the spectral distribution of more energetic photons in the continuous spectrum by differential filters (Lee 1974) (for photon energies  $h\nu < 150$  keV) indicated electron temperatures  $T_e \approx 10$  keV in the same plasma. That the inferred temperature increases with hardness of radiation is to be expected, but these measurements do not lead to a reasonable temperature for the plasma point. Spectral methods should be sufficient to distinguish plasmas with thermal, Maxwellian electron distributions from those with nonthermal but isotropic distributions (Pereira 1988a), or from thermal plasmas with an admixture of directional electron beams.

### 1. Temperature diagnostics with satellites of resonance lines

The plasma temperature can be found from the x-ray spectrum in various ways. Some methods use the continuous part of the spectrum, others employ line intensities of

highly stripped ions. For a transient plasma, such as the plasma point, one should select a method that is unaffected by time variation in plasma properties. The relative intensities of resonance lines and their dielectronic satellites (Gabriel 1972a) depend on temperature but not on ionization equilibrium in the plasma. Thermometry with this method, often used for the H- and He-like lines, is therefore ideal for transient plasmas, provided that the electron distribution is still Maxwellian.

For a "coronal" plasma the radiative decay of the resonant levels dominates over all types of collisional deexcitation. The intensity of the resonant line  $I_r$  in a coronal plasma is then proportional to the collisional excitation rate of the process  $1s^2 + e \rightarrow 1s2p + e'$ . Often the principal channel for excitation of the satellite is dielectronic capture of a free electron by a He-like ion in the ground state,  $1s^2 + e \rightarrow 1s2e2e'$ . Then both the resonant line and the satellites are excited from the same ground state,  $1s^2$ , and the relative intensity  $I_{\text{sat}}/I_r$  of the satellite line does not depend on the ionization state of the plasma. In addition, this ratio does not depend on the electron density (in the coronal case), and is most suitable to determine the electron temperature of the plasma.

Another excitation mechanism for doubly excited He-like ions is collisional excitation of the inner-shell of a Li-like ground state,  $1s^22l + e \rightarrow 1s2l2l' + e'$ . When this mechanism dominates the intensity ratio of satellites to the resonance line gives information on the ionization state of the plasma, more specifically about the relative population of Li- and He-like ions. The temperature of the plasma obtained in this case is called the "ionization temperature"  $T_z$  (Gabriel 1972b). In stationary equilibrium  $T_e = T_z$ . For most real sources the values  $T_e$  and  $T_z$  differ, which suggests that plasmas are typically not in equilibrium. The inequality  $T_e > T_z$  indicates that the plasma is ionizing, while  $T_e < T_z$  indicates a recombining plasma (Bhalla 1975).

In general the satellites are excited through both excitation channels, and it requires special effort to separate the contribution of each channel to the line intensity. When the lines strongly overlap, as usual for spectra from plasma points, it is still more difficult to determine the weight of each channel. Figure 2 contains two samples of realistic spectra to be analyzed later.

An elaborate fitting procedure (Kononov 1983; Kononov 1985) is necessary to obtain diagnostic information from strongly broadened and superposed spectra of a group of satellite transitions. This procedure constructs the spectrum from theoretical data for each of the excitation channels, taking into account the superpositions of the lines. The relative contributions needed to match the experimental spectrum then determines  $T_e$  and  $T_z$ . In high-density plasmas the collisional transfer between autoionized states  $1s2l2l'$  causes further distortions of the spectral profile (see below). In turn these distortions can be used to determine the electron density.

The spectra from plasma points in sulphur, in Fig. 2(a), and from nickel in Fig. 2(b), are used as examples of this procedure in the next section.

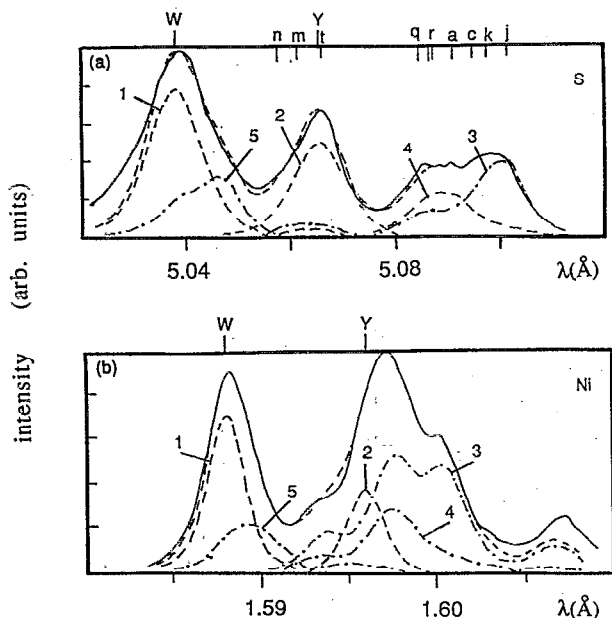


FIG. 2. Spectrum around the resonance line of (a) sulphur; and (b) nickel.

## 2. Measurements of $T_e$ and $T_z$ for elements from Mg to Cu

Kononov *et al.* (1985) used a fitting procedure to find the electron temperature for different compositions of the plasma points in a low-inductance vacuum spark with peak current  $\sim 200$  kA. Spectra of the He- and H-like ions of Mg ( $Z_n = 12$ ), Al ( $Z_n = 13$ ), and S ( $Z_n = 16$ ) were obtained using the 001 plane of a mica crystal ( $2d = 19.9$  Å); for elements from Ca ( $Z_n = 20$ ) to Cu ( $Z_n = 29$ ) the crystal was the quartz 1011 plane, with  $2d = 6.68$  Å. The instrumental line width was  $3 \times 10^{-3}$  Å around 5–9 Å (for Al, Mg, and S), and  $8 \times 10^{-4}$  Å in the region 1–3 Å (for Ca to Cu). These spectra are from up to 100 shots using a focusing crystal spectrograph in Johann geometry.

Figure 2(a) shows the spectrum (solid line) close to the resonance line of He-like S, and Fig. 2(b) gives the spectrum around the He-like resonance line of Ni. The unmarked dashed line gives the best fit; also shown are the contributions of some of the individual transitions in the marked dashed lines: "1" indicates the resonance line  $1s^2(^1S_0) - 1s2p(^1P_1)$ , and "2" the intercombination line  $1s^2(^1S_0) - 1s2p(^3P_1)$ . The broad structure "3" is the superposition of different satellite lines excited by dielectronic recombination, of which the "j" satellite is the strongest. The dashed line "4" is the intensity of the satellites due to collisional excitation of the K shell of the Li-like ground state, while "5" is the dielectronic satellite with principal quantum number  $n$  of the spectator electron  $n \geq 3$ , ( $1s^2nl - 1s2pnl$ ). Their intensities are needed because these transitions form a strong long-wavelength wing to the resonance line, and may contribute significantly to its intensity. The calculated position (Vainshtein 1978) of the most intense satellites on the long-wavelength side of the resonance line (at 5.037 Å) for S, and 1.587 Å for Ni are

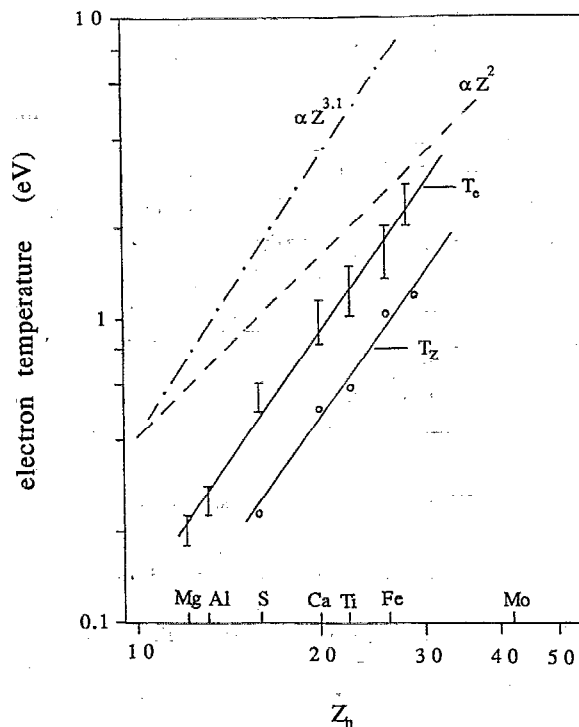


FIG. 3. Plasma point temperatures vs atomic number (or element). The bars come from the fitting procedure, the circles from the Li/He-like line ratio, and the dashed lines from the continuum (see text).

shown above the figure in the designation of Gabriel (1972b).

The spectra of Fig. 2 illustrate the complexity that can be treated. For other atoms, such as magnesium and aluminum, the satellite and resonance lines overlap little, and the electron temperature  $T_e$  can be obtained immediately from the relative intensity of the "j" satellite.

The bars in Fig. 3 give the electron temperature  $T_e$  as measured for many different elements (Kononov 1985). Within experimental error (about 10% due to densitometry and 20% from uncertainties in atomic modeling), the dependence of  $T_e$  on the nuclear charge  $Z_n$  is well described by

$$Z_n \approx 4.5 \times (Z \text{ eV}). \quad (\text{II.1})$$

The circles in Fig. 3 give the ionization temperature  $T_z$  determined by the relative abundance of Li- and He-like ions,  $T_e(\text{Li/He})$ . For all elements  $T_z$  turns out to be considerably smaller than the electron temperature inferred from the satellites to the resonance line of the He-like ion  $T_e(\text{He})$ . As already noted,  $T_e > T_z$  suggests that the plasma point is being heated and ionized.

The electron temperature can also be determined from the relative intensity of satellites to the resonance line of the H-like ion. The electron temperature  $T_e(\text{H})$  for iron turns out to be  $T_e(\text{H}) \approx 4.5$  keV (Kononov 1977), much larger than the value  $T_e(\text{H}) \approx 1.7$  keV measured with satellites to the helium-like resonance line. The relative intensities of the resonance transitions for H- and He-like ions,  $I_{\text{H}}/I_{\text{He}}$ , also gives an ionization temperature for the ioniza-

tion equilibrium between these two ionization states,  $T_z(\text{He}/\text{H})$ . However, in these experiments the electron temperature  $T_e(\text{H}) \simeq 4.5$  keV agrees with the ionization temperature  $T_z(\text{He}/\text{H}) \simeq 4$  keV (Kononov 1977), and with values from other investigators,  $T_z(\text{He}/\text{H}) \simeq 4.3$  keV (Negus 1979), and  $T_z(\text{He}/\text{H}) \simeq 4$  keV (Schwob 1972).

The older results are generally obtained using multiple overlapping spectra from many (typically 100) different shots. However, when comparing different single shots it turns out that  $I_{\text{H}}/I_{\text{He}}$  varies much more from discharge to discharge than other intensity ratios used for diagnostics (Schultz 1989). The disparity between the results obtained by use of various methods will be considered below in discussing theoretical ideas on the nature of plasma points.

### 3. Measurement of the electron temperature with differential filters

We already noted that an iron plasma point gives a continuous spectrum up to photon energy  $h\nu \simeq 150$  keV. The continuous spectrum, often measured through differential filters, can also be used to define an electron temperature  $T_e(f)$ . For the iron pinch mentioned the continuous spectrum corresponds to an electron temperature  $T_e(f) \simeq 10$  keV (Lee 1974; Lee 1975). More recently, Burhenn (1984) measured the electron temperature in the plasma point as function of plasma composition. For iron the measurements give two different temperatures  $T_e(f) \simeq 2.7$  keV and  $T_e(f) \simeq 8.5$  keV, depending on the type of discharge. The dashed line in Fig. 3 displays the cooler temperature as function of the element in the plasma: it is given quite well by  $T_e(f) \simeq 4Z_n^2$  (eV). The hotter temperature, the dot-dashed line in Fig. 3, is approximately given by  $T_e(f) \simeq 0.32Z_n^{3.1}$  (eV).

The separate dependence of the temperature on atomic number suggests that there exist two types of discharges, each with its own dependence on atomic number. Other data (Antsiferov 1989) to be discussed later lead to the identification of two classes of plasma points, small and large. It turns out that  $T_e \sim Z_n^2$  corresponds to the small plasma points while the  $T_e \sim Z_n^{3.1}$  dependence reflects the radiation generated by an electron beam that occurs in a large plasma point.

### C. The electron density of the plasma point

It has proven difficult to determine the electron density in the plasma point, let alone its spatial and temporal dependence. The first estimates, based on Bennett equilibrium for the plasma (Lee 1974), suggested  $n_e \sim 10^{21}/\text{cm}^3$  for an iron plasma. Comparing the x-ray emission of the plasma point with theoretical calculations of radiation loss (Negus 1979) gives somewhat higher values,  $n_e \sim 3 \times 10^{21} - 2 \times 10^{22}/\text{cm}^3$ . Further experimental study led to a reexamination of these estimates. Lee's 1974 estimate was based on a plasma point radius  $r \sim 15 \mu\text{m}$  and a plasma temperature  $T_e \sim 8$  keV, but later it became clear that the radius of a plasma point in a "normal" regime of pinching is less than  $2 \mu\text{m}$  for iron, and that the electron temperature  $T_e$  is about 2 keV (from dielectronic satellites). Using

these data increases Lee's estimate for  $n_e$  by two orders of magnitude, to  $n_e \sim 10^{23}/\text{cm}^3$ . The electron density estimate by Negus (1979) is also based on too large a value of the plasma point volume,  $\Delta V \simeq 4 \times 10^{-10} \text{cm}^3$ , and on too high a temperature ( $T_e \sim 4.3 - 7$  keV). The improved values for the plasma point volume and temperature used with the original radiated power (Negus 1979) now suggests  $n_e \gg 10^{23}/\text{cm}^3$  for iron, in agreement with the more recent data discussed in this review.

An interesting observation is a peak in optical radiation at  $\lambda \sim 760$  nm (Cilliers 1975). Interpreting this peak as collective bremsstrahlung radiation at twice the plasma frequency suggests an electron density  $n_e \simeq 5 \times 10^{20}/\text{cm}^3$ . However, the optical light need not come from the high-density stage of the plasma point, but may reflect other stages of the discharge.

Until recently the only spectroscopic measurements of the electron density of the plasma point were done by Datla (1978/9), who used Stark broadening of the Rydberg lines in H-like and He-like magnesium and aluminum. Using He-like and H-like ions ensures that the information comes from the high-temperature stages of the evolution of the plasma point, when their emission is maximum. The result was  $n_e \simeq 5 - 10 \times 10^{21}/\text{cm}^3$ . However, it was realized later that a significant part of the line broadening is due to the radial size of the plasma: the corrected value turns out to be around  $n_e \simeq 2 - 3 \times 10^{21}/\text{cm}^3$ .

### 1. The electron density from collisional redistribution of satellite transitions

As already noted, some spectral methods give the temperature of a specific phase in the development of the plasma point. Likewise, the electron density should be measured only while the plasma is hot. The satellite spectrum changes with electron density by collisional transfer between the autoionizing states  $1s2l2l'$ . This effect in Li-like calcium and titanium was used to determine the electron density for a plasma point (Kononov 1980). A density effect was already observed in the satellite spectra of H-like Al and Mg in a laser-generated plasma (Bayanov 1976; Vinogradov 1977).

In the limit of small densities the population of the autoionized levels  $n_{ai}$  is determined by

$$n_{ai} = n_{ai}^* \times \frac{\Gamma_i}{\Gamma_i + A_i} \quad (\text{II.2})$$

Here  $n_{ai}^*$  is the Saha-Boltzmann equilibrium population of the autoionizing state with respect to the ground state: for Li-like ions this is the He-like  $1s^2$ . Also  $\Gamma_i$  is the autoionization rate, and  $A_i = \sum_j A_{ij}$  is the total radiative decay rate, the sum of all possible decay rates  $A_{ij}$  from level  $i$  to level  $j$ . For a metastable level ( $i = 1$ ) the radiative decay rate is small,  $A_1 \ll \Gamma_1$ , and the population is close to equilibrium,  $n_1 \simeq n_1^*$ . At the same time, for a level ( $i = 2$ ) with fast radiative decay,  $\Gamma_2 \ll A_2$ , the population can be much less than the equilibrium,  $n_2 \sim n_2^* \times (\Gamma_2/A_2) \ll n_2^*$ .

In a plasma with sufficiently high electron density one must include the transfer of excitation between levels as a result of electron-ion collisions. In a two-level approxima-

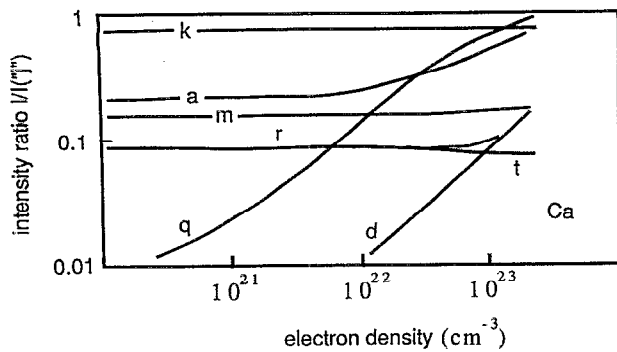


FIG. 4. Intensity of various satellites of calcium with respect to the resonance line, as function of electron density.

tion this effect leads to (collisional) transfer of an excited level from a metastable level (1) to a radiating level (2), which appears as an increased intensity of the corresponding (2) satellite. Calculations show that the “q” satellite is particularly sensitive to collisional transfer effects, and thus to the electron density.

Kononov *et al.* (1980) determine the effect of electron density on the relative population of the satellites using all possible collisional transfers between the levels  $1s2s^2$ ,  $1s2s2p$ , and  $1s2p^2$  of calcium. In stationary state this leads to a system of linear algebraic equations:

$$n_{ai} \times \left( \sum_j A_{ij} + \Gamma_i + n_e \times \sum_j C_{ij} \right) - n_e \times \left( \sum_j n_{aj} C_{ji} \right) = \omega_i \Gamma_i \quad (\text{II.3})$$

Here  $C_{ij}$  is the rate of collisional transfer from state  $i$  to  $j$ , and  $\omega_i$  is the statistical weight of the  $i$ th state. The summations are over the number of levels of the  $1s2l2l'$  configuration.

The results in Fig. 4 come from calculations with 16 levels of calcium, at about 1 keV where He-like calcium is abundant. The figure shows the intensities of calcium’s satellite lines “a,” “d,” “k,” “m,” “q,” “r,” and “t” relative to the intensity of the “j” satellite as function of electron density. In the region of interest,  $n_e \sim 10^{22} - 10^{23} / \text{cm}^3$ , only the “q” and the “d” satellite depend strongly on electron density, with a smaller density effect on the “a” satellite. The “q” satellite is most useful as a density diagnostic because the dependence is relatively strong, changing from 1% to about 100% of the intensity of the “j” satellite in the density region of interest. For higher densities the “a” satellite may also become useful.

The solid line in Fig. 5 gives an experimental spectrum in the region of the resonance line Ca XIX. The solid line at the top of the figure around 3.199 Å (marked 5) is the difference between the experimental spectrum and the computed spectrum without the density effect. The difference curve is located at the theoretical wavelength for the “q” satellite. The shape of the difference is reminiscent of the computed single line profile, which suggests that the observed difference can be accounted for by increasing the intensity of the “q” satellite by increasing the electron den-

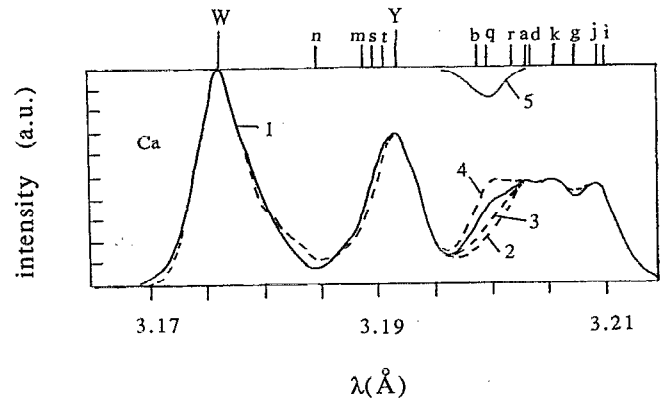


FIG. 5. Calcium spectrum (solid line) around the resonance line (W), the intercombination line (Y), and the satellite lines, with various fits for different densities (dashed lines): 1:  $n_e < 10^{20} / \text{cm}^3$ ; 2:  $n_e = 10^{22} / \text{cm}^3$ ; 3:  $n_e = 3 \times 10^{22} / \text{cm}^3$ ; 4:  $n_e = 10^{23} / \text{cm}^3$ ; Solid line 5 (on top) is the difference between the measured spectrum and the spectrum computed without the density effect.

sity. The dashed lines in Fig. 5 are the theoretical spectra computed for electron densities  $10^{22} / \text{cm}^3$  (curve 2),  $3 \times 10^{22} / \text{cm}^3$  (curve 3), and  $10^{23} / \text{cm}^3$  (curve 4). The best fit to the experimental spectrum is obtained for  $n_e \approx 5 \times 10^{22} / \text{cm}^3$ . Analogous measurements of electron density were made for a titanium plasma, with similar results. The density determination using the “q” satellite (Kononov 1980) was apparently the first direct evidence for an extremely high electron density in the plasma point, on the order of  $10^{23} / \text{cm}^3$ .

For plasma points with heavier elements such as iron ( $Z_n = 26$ ), nickel ( $Z_n = 28$ ) or copper ( $Z_n = 29$ ) the density can, unfortunately, not be found from the “q” satellite, because for these elements this line overlaps with the intercombination line “y” of the He-like ion, the  $1s^2(1S_0) - 1s2p(3P_1)$  transition.

The procedure has been used with other K lines. For example, the density dependence of the satellites to the resonance line of the H-like ion Ti XXII (Seely 1984) gives  $n_e \sim 1.5 \times 10^{23} / \text{cm}^3$ , in good agreement with the above-described measurements. Other measurements show that the density increases with nuclear charge, from about  $3 \times 10^{21} / \text{cm}^3$  for Al, to  $10^{23} / \text{cm}^3$  for Ca and Ti, and  $> 10^{23} / \text{cm}^3$  for Fe.

Like the other parameters of the plasma point the density changes in time. However, each spectral line occurs only during a specific state in the evolution of the plasma. Determining both temperature and density from the same spectral data preserves the proper relation between  $T_e$  and  $n_e$  during the collapse process.

#### D. Investigation of pinch dynamics

The first space-time study of the plasma point in the low-inductance vacuum spark was done with high-speed photography in visible light (Lee 1971; Lee 1974). These experiments showed the beginning stage of the pinching of the discharge channel after filling the inner electrode space by high-conductivity plasma. It was shown that the pinch-

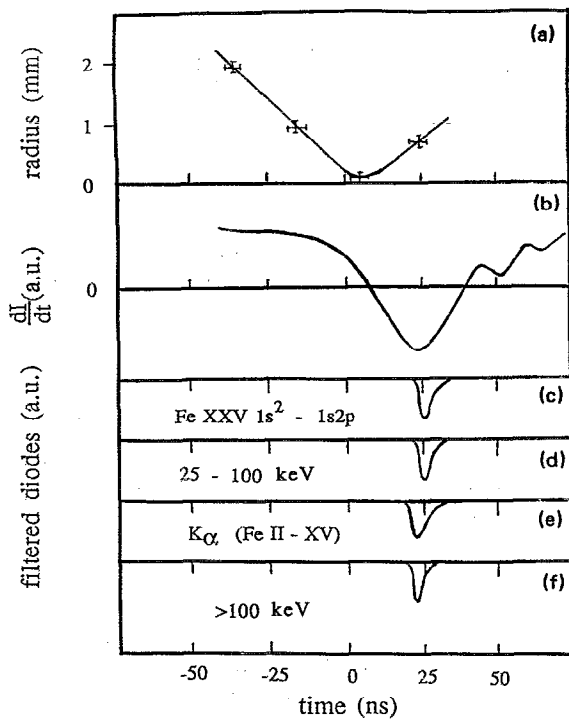


FIG. 6. Temporal characteristics of the low-inductance vacuum spark discharge: (a)  $r$ - $t$  diagram of the pinching of the plasma in the region of the pinch and characteristic oscillograms; (b) derivative of the discharge current; (c)–(f) x-ray pulses of the low-inductance vacuum spark in various energy bands. The time  $t=0$  corresponds to the beginning of emission of the resonance line Fe XXV, i.e., to the moment of formation of the micropinch.

ing was local, producing a constriction. However, the space-time resolution of this method is insufficient to observe compression of the plasma to less than 1 mm. Laser shadowgraphy with five frames, together with time-correlated observation of the current and x-ray pulses in various photon energy bands (Veretennikov 1981a; 1981b), gives a quite complete picture of the compression of the plasma column up to the formation time of the plasma point and its breakup.

The shadowgrams typically show an  $m=0$  Raleigh–Taylor instability. In the early stage of the discharge the radial velocity  $v_r$  is approximately  $v_r \approx 10^6$  cm/s, increasing to  $\approx 5 \times 10^6$  cm/s close to the time of minimum radius when the neck is formed.

Figure 6(a) shows a composite  $r$ - $t$  diagram, obtained from many different shadowgrams of an iron pinch, with error bars indicating the temporal and spatial resolution of 1.5 ns and 100  $\mu\text{m}$ : note that this measurement does not resolve the minimum size of the pinch in K light (see Fig. 1). Figure 6(b) is a typical trace of the current derivative  $dI/dt$ . The current reaches its maximum ( $dI/dt=0$ ) around the time of the minimum radius, while  $dI/dt$  is minimum about 25 ns thereafter.

Figures 6(c)–6(f) contain the x-ray pulses from this pinch correlated to within 0.5 ns time resolution with the current trace of Fig. 6(b). The x-ray is resolved in four rough energy bands, viz., Fig. 6(c) resonance lines of he-

lium-like Fe xxv and their satellites (1.84–1.87  $\text{\AA}$ ); Fig. 6(d): hard x rays with photon energies  $h\nu=25$ –100 keV; Fig. 6(e):  $K_\alpha$  radiation of ions of low ionization multiplicity (1.93–1.96  $\text{\AA}$ ); and Fig. 6(f): hard x rays with  $h\nu > 100$  keV.

The harder x rays appear from 15 to 25 ns after the occurrence of the minimum radius as seen in the shadowgram, and the current maximum. This timing indicates that the plasma point forms about 20 ns after maximum compression. A separate x-ray pinhole photograph shows that the plasma point sits in the neck of the pinch.

The beginning of the characteristic  $K_\alpha$  radiation from the partly stripped ions Fe II to Fe xvii, Fig. 6(e), coincides with the emission of x rays in the hard x-ray band  $h\nu > 100$  keV, Fig. 6(f). However, this pulse starts typically 3 ns before the beginning of the x-ray pulse in He-like resonance lines of Fe xxv stripped to the K shell, Fig. 6(c): this last pulse coincides with the x-ray pulse in the photon energy range 25–100 keV, Fig. 6(d). These data are similar but more precise than earlier observations on a copper pinch (Lee 1974).

The electron temperature and density inferred from the data in Fig. 6 do not match the spectroscopic measurements. The pinch region in the shadowgram is opaque because the light frequency  $\omega_0$  is less than the plasma frequency  $\omega_e = \sqrt{n_e e^2 / \epsilon_0 m}$  (Veretennikov 1981a,b). This leads to a lower limit for the electron density on axis,  $n_e \geq 10^{20}/\text{cm}^3$ . Another estimate is obtained from the pinch size in VUV light as displayed in Fig. 1. A  $\sim 100$   $\mu\text{m}$  radius corresponds to 0.5-keV photon energy and 0.2-keV temperature. The Bennett relation (with  $I \approx 200$  kA) then gives  $n_e \approx 2 \times 10^{21}/\text{cm}^3$ . A similar upper limit to the density,  $n_e < 10^{21}/\text{cm}^3$ , has been obtained by conservation of line density during compression of an initially tenuous plasma (Negus 1979). In contrast, spectroscopic measurements using the resonance lines of high- $Z$  ( $Z_n$  20–30) elements give densities of  $n_e \sim 10^{23}/\text{cm}^3$  and temperatures  $T_e \sim 2$  keV (see Fig. 1).

The different data can be reconciled by a model with two compression stages. The first stage, the relatively slow hydrodynamic compression seen by the shadowgraphy, creates a neck of warm plasma and the conditions for a second compression. This second compression is consistent with the radiative collapse model of Vikhrev (1982a) as described in Sec. III below. Radiative collapse creates the plasma point.

In the hydrodynamic compression stage the plasma heats up to a moderate temperature consistent with the occurrence of partly stripped ions like Fe II to Fe xvii:  $K_\alpha$  radiation from these ions and hard x rays with  $h\nu > 100$  keV indicates that nonthermal processes occur in addition. Subsequently, the plasma point develops. This second stage takes place on a fast, nanosecond-like timescale inside the plasma neck. Its hot, dense plasma is consistent with the emission of resonance lines of He-like Fe xxv, and with x rays in the 25–100 keV energy range.

The second compression stage leading to the plasma point is faster ( $< 100$  ps) than the response time of the diagnostics for Fig. 6. A soft x-ray emission time of 60–100

ps was estimated with a fast x-ray streak camera, indicating that the hot phase of the plasma point is comparably short (Peacock 1968). Aglitski *et al.* (1985) used high-resolution spectroscopic equipment for a precise measurement of the line shape and position of the resonance line of He-like iron. The shape of the lines indicates Doppler broadening from radial expansion (or contraction) with velocity  $v_r \sim 2-3 \times 10^7$  cm/s, while the Doppler shift suggests a velocity for the total plasma point of less than  $v_p \sim 10^7$  cm/s. From the apparent size of the plasma point, about  $r_p \sim 2 \mu\text{m}$ , they conclude that the radiation lasts about  $r_p/v_p \sim 20$  ps.

The remainder of this review describes the radiative collapse of the plasma into a plasma point in more detail, principally from the theoretical side but with reference to experimental data where appropriate.

### III. RADIATIVE COMPRESSION MODEL FOR THE PLASMA POINT

A successful model for the plasma point must explain its high ( $\sim 2$  keV) temperature, high ( $\sim 10^{23}/\text{cm}^3$ ) electron density, small ( $\lesssim 10 \mu\text{m}$ ) size, and short ( $\sim 30$  ps) lifetime. Presently the most developed model for the plasma point is a radiative collapse theory in the form proposed by Vikhrev *et al.* (1982a). In an approximate way this theory reproduces the scaling of the plasma point parameters with the atomic number of the pinch material. In a radiative collapse the plasma point is heated by compression and Joule heating. Beams of high-energy electrons are considered a minor influence for the energetics, and they are not part of the model. Below we discuss the radiative compression model in some detail.

Over the years certain aspects of plasma points have been explained in different ways. An early theory assumed that the plasma points are electrode dust ejected and heated by an electron beam (Negus 1979). A plasma point-sized microparticle with a 0.01 mm diameter is easily heated by a 100 kA beam of 10 keV electrons, or a fluence of  $10^{15}$  W/cm<sup>2</sup>. Getting to keV-like temperatures demands no more than  $\sim 10^{16}$  W/cm<sup>3</sup>, allowing for a deposition length of 1 mm along the pinch axis in agreement with the elongated shape of the plasma point.

However, other observations contradict this model. Beam heating predicts pancake-shaped plasma points, because 10 keV electrons penetrate only a fraction of a micron into a solid. Also, a plasma point heated by fast electrons would be the source of the hard x rays, while in experiments the hard x-ray emission comes from between the plasma point and the anode. And in gas-puff z pinches electrode-generated microparticles should not appear, but the gas-puff pinches do show plasma points.

Other explanations of the plasma point emphasize the radiation produced by electron beams, i.e., plasmas with non-Maxwellian and anisotropic electron energy distributions. There is no doubt that electron beams exist in low-inductance vacuum spark discharges (Welch 1974; Choi 1987). In other discharges electron beams have been measured directly (Kania 1984) and inferred from spectroscopic data (Hammel 1984; Hares 1985). In the theoretic

cal approach we favor, the radiative collapse model, the electron beams do not cause the plasma point, but the plasma point could create an electron beam. Electron beams are mentioned in this review solely for their effect on the radiation.

In our opinion the radiative collapse model is the only reasonably complete approach that accounts for the formation of plasma points. For this reason we spent the bulk of this review on an account of this model, and a discussion of the relevant experimental data.

### A. Historical development of plasma point theory

Various aspects of plasma point formation with compression and Joule heating were first formulated in connection with research on nuclear fusion with deuterium pinches. In these experiments the dense plasma located on the axis of the discharge produces soft x rays, accompanied by neutrons and high-energy ion and electron beams (Filipov 1983; Trubnikov 1976).

A uniform hydrogen pinch in radial force equilibrium (Bennett 1934) has a critical current determined by power between Joule heating and optically thin bremsstrahlung (Pease 1957; Braginskii 1957). The Pease-Braginskii current for hydrogen,  $I_{PB}^H \approx 1.6$  MA, applies to fusion-like parameters with a Coulomb logarithm  $\sqrt{\ln \Lambda} \approx 10$ . For other plasma parameters  $I_{PB}^H$  changes weakly with the Coulomb logarithm. Apart from the weak dependence on plasma parameters through the Coulomb logarithm the Pease-Braginskii current does not depend on the temperature  $T$  because Joule heating and bremsstrahlung both increase with temperature as  $T^{1/2}$ , at least when line density, current, and temperature are connected by the Bennett relation  $NT \propto I^2$ . Likewise, with decreasing radius  $r$  both Joule heating and optically thin radiation increases as  $1/r^2$ , and the pinch radius drops out of the power balance. Joule heating and optically thin radiation do not determine an equilibrium radius.

For atoms other than hydrogen  $I_{PB}^Z$  is a function of the nuclear charge of the ions  $Z$  through a factor  $1 + 1/Z$ . For ions with  $Z_n \gg 1$  the top lines in Fig. 7(a) show  $I_{PB} \approx 0.8$  MA, for  $\ln \Lambda = 10$ . In what follows the weak dependence on the Coulomb logarithm is neglected because its influence is on the same order as the many other approximations.

For fusion plasmas bremsstrahlung dominates the radiation loss, but this is not the sole radiation process. In extremely hot and dense plasmas synchrotron radiation can be balanced against Joule heating (Korop 1979). The resulting equilibrium, with  $I \sim 100$  kA, is unstable. At sufficiently small plasma radius ( $\sim 1$  nm) electron degeneracy effects appear, synchrotron radiation loss begins to exceed Joule heating power, and the plasma cools. Cooler plasma implies reduced pressure, and further contraction of the plasma: the plasma collapses. In this theory, the average energy of the particles before the collapse is already several hundreds of keV, at a plasma density of  $10^{30}/\text{cm}^3$ , and synchrotron radiation emitted during the collapse is in the hard x-ray regime as observed in x-ray bursts from plasma points. These considerations and related ideas

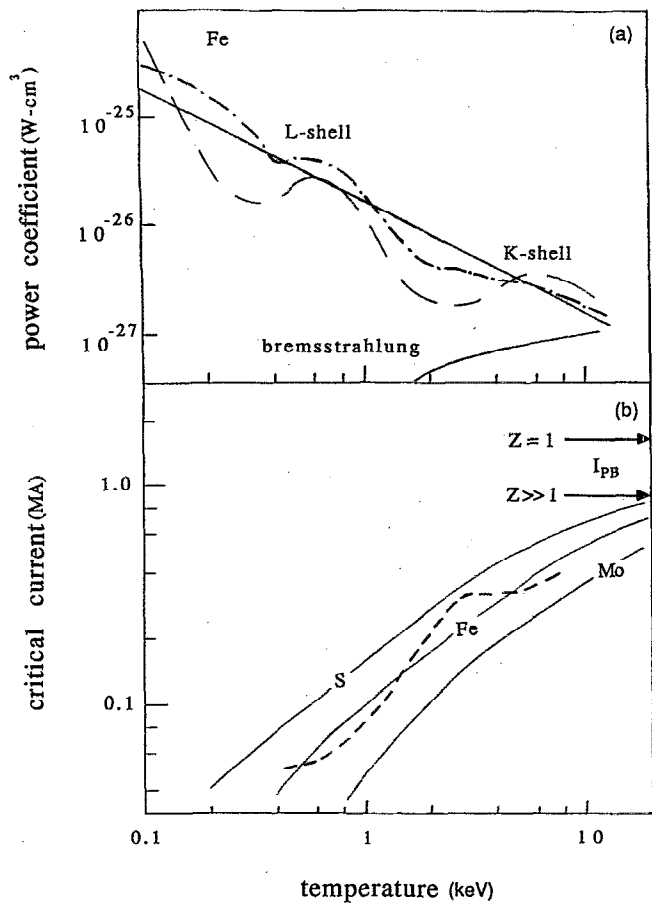


FIG. 7. (a) Power coefficient in iron line radiation vs plasma temperature. The dashed line are computations by Jacobs, the dash-dot line by Breton. The solid line is the approximation used later. Bremsstrahlung (at bottom) can be ignored. (b) the Pease-Braginskii current based on Jacobs' power coefficient for iron (dashed line), and for the approximate model (solid). Approximate values for sulphur and molybdenum are also given. The arrows at left give  $I_{PB}$  for hydrogen, and  $I_{PB}$  for  $Z \gg 1$  in the limit of complete ionization.

(Meierovich 1984; Meierovich 1986) were important in clarifying the phenomenon of radiative collapse, although we now know that plasma turbulence and the associated anomalous heating prevents the supercompressed state to be reached from normal physical parameters (e.g.,  $n_e \sim 10^{23}/\text{cm}^3$  and  $T \sim 1$  keV). Radiative collapse in hydrogen pinches continues to be investigated including these additional effects (e.g., Chittenden 1989; Giuliani 1989; Robson 1989a).

In plasmas with atoms of higher atomic number  $Z_n \geq 10$  and thermodynamic parameters relevant to vacuum sparks the power loss from bound-bound and free-bound transitions exceeds the bremsstrahlung power by a large factor,  $K(T; Z_n)$ . As a result the Pease-Braginskii current  $I_{PB}$  is less than  $I_{PB}^H$  for hydrogen:  $I_{PB}(T; Z_n) = I_{PB}^H / \sqrt{K}$ . The function  $K$ , which depends on detailed atomic physics considerations, is available in the literature (e.g., Post 1977):  $I_{PB}(T; Z_n)$  has been computed for some elements with these data (Shearer 1976; Negus 1979; Vikhrev 1982a). Figure 7(a) shows  $I_{PB}(T; Z_n)$  as function of temperature for sulphur, iron, and molybdenum

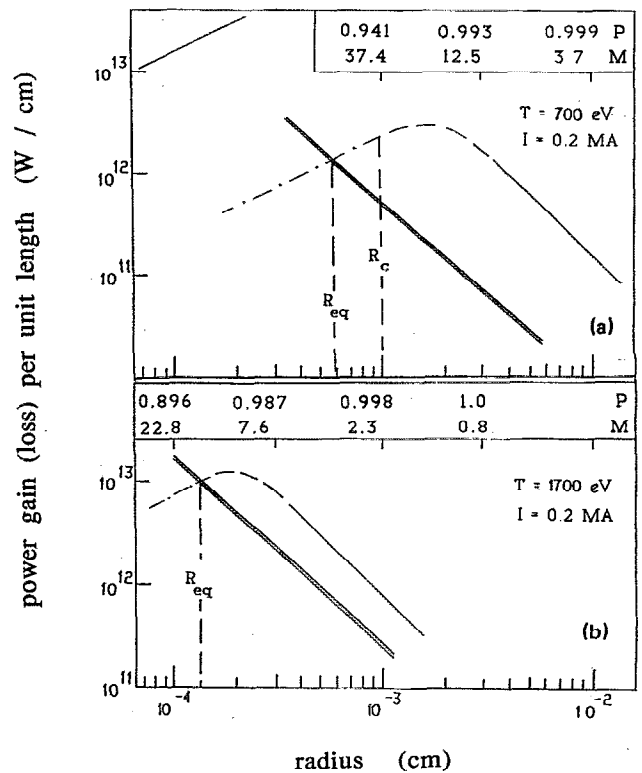


FIG. 8. Power per unit length as function of radius for an iron pinch with 0.2 MA in equilibrium at two line densities and two corresponding temperatures, (a) 700 eV; and (b) 1700 eV. The double line is Joule heating, the solid-dashed line is the radiative power loss. The equilibrium radius is given by the intersection of the two curves. See text for numbers on top.

( $Z_n = 16, 26,$  and  $42$ ).

Reabsorption of radiation turns out to be important in the vacuum spark plasma: the plasma is optically thick for the relevant parameters  $T_e \sim 1-10$  keV and  $n_e \sim 10^{23}/\text{cm}^3$  or  $n_i \sim 10^{22}/\text{cm}^3$ . A cylinder of tenuous plasma emits optically thin volume radiation, which varies with radius as  $1/r^2$ . In the opposite extreme, blackbody radiation, the radiation depends only on the emitting area. Then the radiation per unit length increases linearly with radius,  $P_{BB}/l = 2\pi r \sigma_{SB} T^4$  (the Stefan-Boltzmann constant  $\sigma_{SB} \approx 10^5$  W/cm<sup>2</sup> eV<sup>4</sup>). In reality, the total energy loss by radiation for intermediate plasma radii varies smoothly, from  $1/r^2$  for large  $r$  to a linear increase with radius for small  $r$ . However, for our relatively small plasmas the surface radiation loss is still one or two orders of magnitude less than for an ideal blackbody. Figure 8, to be discussed later, illustrates the energy loss as function of radius for two temperatures in iron: the blackbody radiation loss is visible in the upper left corner (for 700 eV). Unlike optically thin radiation, the equilibrium between optically thick radiation with Joule heating does give an equilibrium radius for the pinch,  $r_{eq}$  in Fig. 8.

These equilibrium estimates assume that the plasma is radially uniform in current density, particle density, and temperature. Of course, none of these is necessarily true in reality, in part because these conditions are inconsistent with pressure and energy balance. As an example, radial

structure changes the radiation output, and affects the resistivity (Robson 1989b). Despite these inconsistencies a uniform plasma is a frequent approximation that should be reasonable in many cases (except for plasmas with a dense, cold core and a tenuous, hot periphery when the opposite approximation would be more reasonable).

A typical pinch is hydromagnetically unstable to axial perturbations. The sausage mode creates the conditions for radiative collapse. The basic idea is that the neck of a hydromagnetic sausage instability forms a plasma column of smaller size (Book 1976). Collapse can proceed when the energy loss from radiation in a characteristic instability time,  $\tau \sim r/v_A$  ( $v_A$  is the Alfvén speed at the edge of the pinch), exceeds the heat content of the plasma (Shearer 1976; Winterberg 1978); equivalently, the radiation power per unit length of the plasma must be larger than the energy loss due to expulsion of plasma from the pinch (Vikhrev 1978a; Vikhrev 1978b). It is important to realize that the plasma increases the value of  $n_e\tau$  during compression (Vikhrev 1977; Vikhrev 1978a). This guarantees that the radiative power continues to exceed the energy lost by plasma expulsion, and the plasma column can continue its radiative collapse.

These concepts, atomic radiation with opacity and axial outflow of plasma, are the core of a simplified, zero-dimensional model for the plasma point (Vikhrev 1982a), the radiative collapse model. The simplifications make it possible to follow the entire process of radiation collapse in time, in an approximate way. Although more accurate modeling can be done for 2D hydrodynamics, opacity, and ion kinetics in isolation, it is barely possible to integrate all these aspects into one single computation. The most detailed computations to date either have little radiation (Lindemuth 1990) or contain a conceptually complete radiation package (but without radiation transport) that is constrained by computation considerations (Cochran 1990). Eventually, as resources increase these and similar computations will supersede the abridged models discussed here.

Vikhrev's model appears to contain the phenomena that dominate the life of the plasma point: it successfully predicts plasma temperature, density, and plasma point lifetime. In addition there are experimental indications that plasma outflow is related to the plasma point (Hares 1984; Stewart 1987).

## B. Model for radiation compression of a high-Z plasma

This section introduces the general ideas of the radiative compression model as well as some quantitative results from a simple analytical model (Koshelev 1985). This analytical approximation seems to provide a good qualitative (and for many cases quantitative) description of the process. The next section presents results for a more complete model that includes the hydrodynamics of the plasma and a more exact form for the radiative energy loss.

## 1. Critical current

Force balance in the radial direction (Bennett 1934) gives a simple relation between the line density for electrons,  $N_e = \pi r^2 n_e$ , the electron temperature  $T_e$ , and the total current  $I$ . The Bennett relation is

$$\frac{\mu_0 I^2}{4\pi} = (Z_{\text{eff}} + 1) N_i k T. \quad (\text{III.1})$$

The left-hand side is the linear energy density of the magnetic field for a total current  $I$ , and the right hand side is the linear kinetic energy of the plasma, with  $N_i$  the number of ions per unit length, and  $T$  the plasma temperature (assumed equal for ions and electrons): the electron line density  $N_e = Z_{\text{eff}} N_i$ . In numerical form,

$$(Z_{\text{eff}} + 1) N_i T = 3.12 \times 10^{21} I^2, \quad (\text{III.2})$$

where  $T$  is the plasma temperature (in eV),  $N_i$  is the number of ions per unit length (in cm) and  $I$  is the pinch current (in MA). The Bennett relation applies when kinetic and magnetic pressure are the only relevant forces, and when the radial velocity of the plasma column is small compared to the sound speed.

Bennett equilibrium deals only with the averaged particle density, temperature, and current density, and says nothing about the value of the radius where the plasma edge is located. Once in equilibrium the external forces on the plasma are balanced, and the plasma edge would remain at the same radial position while the radial profiles of the thermodynamic quantities continue to evolve.

In a hydrogen plasma column in Bennett equilibrium the energy loss by bremsstrahlung balances Joule heating with Spitzer conductivity at the Pease-Braginskii current  $I_{\text{PB}}$  (Pease 1957; Braginskii 1957). A current  $I$  with constant current density produces in a homogeneous plasma of radius  $r$  and average charge state  $Z_{\text{eff}}$  a power  $Q_{\text{Joule}}$  per unit length  $l$  of  $Q_{\text{Joule}}/l = I^2/\sigma A$ . The conductivity  $\sigma = \sigma_0 T^{3/2}/Z_{\text{eff}} \ln \Lambda$  is the Spitzer conductivity,  $\ln \Lambda$  is the Coulomb logarithm, and the pinch area  $A = \pi r^2$ . The constant  $\sigma_0 = 100 \Omega^{-1} \text{cm}^{-1} \text{eV}^{-3/2}$ . Then

$$Q_{\text{Joule}}/l = 3.3 \times 10^9 \frac{Z_{\text{eff}} \ln \Lambda I^2}{T^{3/2} r^2}, \quad (\text{III.3})$$

where  $Q_{\text{Joule}}/l$  is in W/cm, and  $I$  in MA.

As the radius decreases and the density goes up to the assumptions that lead to Spitzer resistivity are no longer true. With more realistic models  $I_{\text{PB}}$  may change a factor  $\sim 2$  (Giuliani 1989; Robson 1989b), on the same order as possible dependences on the Coulomb logarithm. Anomalous heating related to current-driven instabilities is more difficult to estimate, and also more important [see below Eq. (III.29)]. For the moment Eq. (III.3) is sufficient, and convenient in future use.

The radiative power density in bremsstrahlung (or free-free radiation)  $P_{\text{ff}} = X_{\text{ff}} n_e n_p$ , where the free-free power coefficient  $X_{\text{ff}} = 1.4 \times 10^{-32} Z_{\text{eff}}^2 T^{1/2} \text{W cm}^3$ . In Bennett equilibrium the bremsstrahlung power loss per unit length is

$$Q_{ff} = 4.3 \times 10^{10} \frac{Z_{\text{eff}}^4 I^4}{T^{3/2} r^2}, \quad (\text{III.4})$$

for  $Z_{\text{eff}} \gg 1$  ( $Q_{ff}$  is in W/cm). This leads to the well-known value for  $I_{\text{PB}} \approx 0.27 (\ln \Lambda)^{1/2}$  MA, for a fully ionized high- $Z$  plasma.  $I_{\text{PB}}$  can also be expressed as the Alfvén current  $I_A \approx 17$  kA multiplied by a factor that compares the cross sections for collisional energy transfer ( $\propto \ln \Lambda$ ) and bremsstrahlung (Pereira 1990).

In reality the current is never constant. Typically,  $I(t)$  has a pulse shape determined largely by the pulse power machinery, with some details reflecting the dynamics of the pinch. Assume for the moment that the pinch has reached equilibrium at a certain current. If the current increases above  $I_{\text{PB}}$  without a corresponding change in temperature the magnetic pressure exceeds the thermal pressure: the plasma contracts. However, Bennett equilibrium can be reestablished due to compressional heating, i.e., the conversion of magnetic field energy to thermal energy. In fact, it is possible to heat the pinch while remaining in Pease-Braginskii equilibrium if the current increases in time as  $I \propto t^{1/3}$  (Haines 1960; Hammel 1976). The hydrogen pinch in variants of these zero-dimensional approximations was discussed recently by Chittenden (1989), Giuliani (1989), and Robson (1989a,b).

In a plasma of heavy ions it is possible to maintain Bennett equilibrium during contraction of the pinch. As the plasma contracts the radiative losses decrease due to opacity and density effects, and the small difference between the radiative losses and Joule heating is easily compensated by magnetic field work.

Energy balance based on bremsstrahlung radiation is relevant to hydrogen plasmas, and to fully ionized high- $Z$  plasmas. However, the majority of ions is fully stripped only at exceedingly high temperatures  $T \gtrsim 3Z^2 Ry$  (e.g., Huddleston 1965:  $Ry = 13.6$  eV is the Rydberg constant). Usually a pinch with high- $Z$  plasma is only partly ionized, line radiation dominates over bremsstrahlung, and  $I_{\text{PB}}^Z$  no longer defines power balance. Instead, power balance occurs at a critical current  $I_{\text{cr}} \ll I_{\text{PB}}^Z$ :  $I_{\text{cr}}$  depends on the thermodynamic variables of the plasma but not on the plasma size, because the plasma is still assumed to be optically thin.

The critical current  $I_{\text{cr}}$  for a plasma of heavy ions is obtained easily from the total radiation loss of a plasma in the form  $P_{\text{tot}} = P_{\text{ff}} \times K(T, Z_n)$ . The factor  $K(T, Z_n)$  is a complicated function of temperature  $T$ , and of nuclear charge  $Z_n$ . Its computation involves detailed atomic physics considerations that fall outside this review. Here  $K(T, Z_n)$  is considered given by the literature (e.g., Post 1977).

In Bennett equilibrium, and assuming uniform current density over the pinch,

$$\frac{I_{\text{cr}}^2}{I_{\text{PB}}^2} = \frac{P_{\text{tot}}}{P_{\text{ff}}}, \quad (\text{III.5})$$

which gives the critical current  $I_{\text{cr}} = 0.27 (\ln \Lambda / K)^{1/2}$ .

Figure 7(b) compares the temperature dependence of the power coefficient  $X_{\text{ff}}$  for bremsstrahlung (lower solid line) with the power coefficient for line radiation  $X_{\text{line}}$

$= P_{\text{line}}/n_e n_i$  for iron ( $Z_n = 26$ ), in three approximations. The dashed line comes from the computation by Jacobs (1977), and the dot-dashed line from Breton (1978). The two computations are similar in the onset of  $L$ -shell radiation (around 0.6 keV) and  $K$ -shell radiation (around 4 keV), but the power coefficients differ by a factor on the same order as the already neglected influence from the Coulomb logarithm ( $\sim 2$ ). Bremsstrahlung becomes important beyond about 5 keV. The solid line is an analytical approximation to  $X_{\text{line}}$  (Koshelev 1985):

$$X_{\text{line}} \approx 4 \times 10^{-29} \frac{Z_n^4}{T}, \quad (\text{III.6})$$

(where  $X_{\text{line}}$  is in  $\text{W cm}^3$ ). This approximation agrees with the more accurate computations to within their differences in the relevant temperature regime (0.3–10 keV). The power loss per unit length in line radiation for a plasma in Bennett equilibrium then becomes:

$$Q_{\text{line}} \approx 1.24 \times 10^{14} \frac{Z_n^4 I^4}{Z_{\text{eff}} T^3} \times \frac{1}{r^2}, \quad (\text{III.7})$$

Balancing radiative power with Joule heating,  $Q_{\text{line}} + Q_{\text{ff}} = Q_{\text{Joule}}$  gives the critical current  $I_{\text{cr}}$ . The dashed line in Fig. 7(a) is the critical current for iron (Fe,  $Z_n = 26$ ): it reflects the variations with temperature seen in Jacobs' power coefficient (dashed line in Fig. 7b).

Bremsstrahlung can safely be ignored up to moderately high temperatures, when  $Q_{\text{line}} \gg Q_{\text{ff}}$ . This approximation gives  $I_{\text{cr}}$  for sulphur ( $S$ ,  $Z_n = 16$ ), iron and molybdenum ( $\text{Mo}$ ,  $Z_n = 42$ ). Analytically

$$I_{\text{cr}} \approx 5 \times 10^{-3} \sqrt{\ln \Lambda} T^{3/4} \frac{Z_{\text{eff}}}{Z_n^2}, \quad (\text{III.8})$$

which is for  $\ln \Lambda \sim 10$

$$I_{\text{cr}} \approx 0.016 \times T^{3/4} \frac{Z_{\text{eff}}}{Z_n^2} \quad (\text{III.9})$$

(where  $I$  is in MA). The deviation from the  $T^{3/4}$  line in Figure 7(a) comes principally from the inclusion of bremsstrahlung at high temperatures, and to a minor degree from the (weak) temperature dependence of the effective atomic number  $Z_{\text{eff}}$ . The Pease-Braginskii current estimated analytically differs by about 50% from the more accurate approximations.

In the following we continue to illustrate the basic physics behind the different pinch phenomena with simple analytical approximations rather than with more precise numerical results. This is partly for clarity, and partly because the broad atomic and radiation physics background falls outside this review. The various estimates that follow are intended to be semiquantitative. Quantitatively correct results must await computations that include all the complications inherent in radiation transport computations: an accurate computation of optically thick radiation has only recently been applied to radiation collapse (Apruzese 1889/1990).

## 2. Equilibrium radius

In an equilibrium pinch optically thin radiation losses vary with radius as  $1/r^2$  only in the low density, "coronal," type of plasma. In the coronal approximation the ions are excited exclusively by collisions with electrons, and all excited ions de-excite only by radiating a photon which leaves the plasma. In contrast, for higher densities collisional de-excitation can be significant. Then the excitation energy is given back to the plasma instead of being radiated out, and the plasma radiates less. Moreover, the radiation varies with radius in a different way because collisional de-excitation depends on density, and therefore on radius.

Consider a plasma wherein the ions have only two energy levels. The spontaneous radiation rate is  $W_r$  and the collisional de-excitation rate by collisions with electrons is  $n_e W_e$ . The total de-excitation rate is then  $W_r + n_e W_e$  compared to  $W_r$  in the coronal plasma. The radiation coefficient decreases by the factor  $W_r/(W_r + n_e W_e)$  to

$$X'_{\text{line}} = X_{\text{line}} \times \frac{1}{1 + n_e W_e / W_r} \quad (\text{III.10})$$

In a low-density plasma,  $n_e W_e \ll W_r$ , the radiation coefficient does not change with density. Then the radiated power  $P \propto n_e n_i \propto n^2$ , and the radiated power per unit length is  $Q = \pi r^2 P$ . For a pinch in Bennett equilibrium, with current  $I$  and temperature  $T$  and a line density  $N = \pi r^2 n$  that remains constant with radius the radiated power per unit length is  $Q \propto I^4 / r^2$ , inversely proportional to the cross-sectional area  $r^2$ . However, in a denser plasma when  $n_e W_e \gg W_r$ , the radiation coefficient  $X' \sim W_r / n_e \times W_r / W_e$  is inversely proportional to the electron density  $n_e$ . Then the radiated power  $P$  is no longer  $P \propto n^2$ , but one of the density factors cancels, and  $P \propto n_i$ . Although the plasma is still optically thin, i.e., the photons are not reabsorbed by the plasma, the radiated power is no longer inversely proportional to  $1/r^2$ . Instead, for a denser but still optically thin plasma the power loss per unit length of a Bennett pinch with given line density becomes  $Q \propto I^2$ , independent of pinch radius  $r$ .

The coefficient for radiative de-excitation  $W_r$  scales with excitation energy, or photon energy  $h\nu$ , as  $W_r \propto (h\nu)^2$  (e.g., Vainshtein 1979). The collisional de-excitation rate  $W_e \sim \nu \sigma_e$  is proportional to some average electron velocity  $\nu$  and the de-excitation cross section  $\sigma_e$ , which scales inversely with average electron energy  $T$  as  $\sigma_e \sim T^{-2}$ . Therefore,  $W_e \propto T^{-3/2}$ . Often the average energy of the photons responsible for most of the plasma radiation is proportional to the temperature,  $h\nu \sim 2kT$ , and  $W_e / W_r \sim (h\nu)^{-7/2} \sim T^{-7/2}$ . The numerical factor in front of these scaling estimates is approximately constant along the isoelectronic sequence but differs for different types of ions (K ions, L ions, ...). For analytical modeling below we use  $W_e / W_r \approx 10^{-14} / T^{7/2} \text{ cm}^3$  for both L shell and K shell, with  $T$  in eV.

A photon escapes from the plasma (and the plasma radiates) if its mean free path  $l_\nu$  is much larger than the plasma radius  $r$ . Otherwise, when the optical depth  $r/l_\nu \gg 1$ , the photon excites a large number  $M$  of ions before it

reaches the plasma edge:  $M \approx r/l_\nu$ . When the radius  $r$  decreases the density of ions in the ground state  $n_i$  increases (assuming constant line density  $N = n_i \pi r^2$ ). The mean free path  $l_\nu \sim 1/n_i$  decreases as  $r^2$ . Thus the number of photon-ion collisions  $M$  increases as  $M \sim 1/r$ .

Without collisional de-excitation each of these ions re-emits the photon in an arbitrary direction. The energy of the re-emitted photon is random with a probability distribution given by the lineshape. All the radiation escapes, but in a broader line. Multiple scattering together with collisional de-excitation deposits the photon energy back into the plasma, and reduces the radiation loss.

The decrease in the radiation rate due to opacity is estimated as follows. The probability  $p$  that a photon is re-emitted in one absorption-emission cycle is  $p = 1/(1 + n_e W_e / W_r)$ . The probability that the photon escapes the plasma without being redeposited is then  $\beta = p^M$ , where  $M$  is the average number of scatterings per photon. For the case of total frequency redistribution inside a Doppler line contour an acceptable approximation is  $M = \alpha r / l_\nu$ , where the parameter  $\alpha$  depends on geometry, optical depth (as  $\ln r/l_\nu$ ) and line profile: typically  $\alpha \sim 5$  (e.g., Holstein 1951).

The mean free path  $l_\nu = 1/n_i \sigma_\nu$ , where  $\sigma_\nu$  is the cross section for absorption of the line photon. This cross section depends strongly on the line width and on the photon energy, and is proportional to the statistical weight  $\omega_g$  of the ground states of the ions that are likely to be present in the plasma, e.g.,  $\omega_g \sim 10$ . Again assuming that  $T \approx 2h\nu$  and using  $n_e = Z_{\text{eff}} n_i$  the mean free path becomes

$$l_\nu \approx 3 \times 10^{13} \frac{Z_{\text{eff}}^{3/2} T^{3/2}}{Z_n^{1/2} n_e} \quad (\text{III.11})$$

with  $l_\nu$  in cm. For a plasma in Bennett equilibrium this becomes

$$l_\nu \approx 3 \times 10^{-8} \frac{Z_{\text{eff}}^{3/2} T^{5/2}}{Z_n^{1/2}} I^2 \quad (\text{III.12})$$

(with current  $I$  in MA and  $r$  in cm).

Figure 8 shows the radiation per unit length for an iron pinch as function of radius. Figure 8(a) is a warm pinch with temperature  $T = 700$  eV and electron line density  $N_e = 18 \times 10^{16} / \text{cm}$  corresponding to Bennett equilibrium for a current  $I = 0.2$  MA. Figure 8(b) is for a hot pinch with  $T = 1700$  eV and reduced mass per unit length  $N_e = 7.3 \times 10^{16} / \text{cm}$ , but approximately the same current (assuming no change in  $\ln \Lambda$  with temperature and density). For the warm pinch the effective atomic number is  $Z_{\text{eff}} = 17$ , and the linear ion density is  $N_i = 10^{16} / \text{cm}$ ; for the hot pinch  $Z_{\text{eff}} = 25$  and the ion density is  $3 \times$  smaller,  $N_i = 0.3 \times 10^{16} / \text{cm}$ . Note that the warm pinch could evolve into the hot pinch by axial outflow of material, but not by compression without outflow.

The solid line is the radiation per unit length for coronal and optically thin radiation, decreasing as  $1/r^2$  with increasing radius. The dashed line shows the reduction in radiation per unit length due to optical thickness, according to the formula  $Q' = Q p^{1+M}$ . The upper number in the

box at the top of the figure is the probability for collisional de-excitation  $p = 1/(1 + n_e W_d/W_r)$ , which decreases with radius through the density  $n_e \propto 1/r^2$ . The probability  $p$  is close to unity and the coronal approximation is well justified up to rather small radius of compression.

The lower number in the box is the number of scatterings  $M$ . The large number of scatterings  $M \gg 1$  combined with small deviations from the coronal approximation,  $p \lesssim 1$ , strongly reduces the radiation per unit length as the pinch contracts.

The critical radius  $r_c$  indicates where the plasma radiation goes over from volume-like to surface-like. This transition should occur approximately when a sizeable fraction of the photons is reabsorbed, e.g., when

$$p^{1+M} \simeq 1/e \simeq 0.37.$$

Assuming  $n_e W_d/W_r \ll 1$  in  $p = 1/(1 + n_e W_d/W_r)$  gives  $p^{1+M} \sim M n_e W_d/W_r$  (using  $M \gg 1$ ), and this gives a critical radius

$$r_c \simeq 1.2 \times 10^5 \frac{I^{4/3} Z_n^{1/6}}{Z_{\text{eff}}^{1/2} T^{7/3}}, \quad (\text{III.13})$$

with  $r_c$  in cm.

The radiative losses are assumed to be surfacelike for plasma smaller than the critical radius. Then  $Q_s \simeq Br$ . The coefficient  $B$  can be obtained by setting  $Q_s = Br$  equal to the estimate  $Q' = Qp^{1+M}$  at the critical radius:

$$Q_s \simeq 0.027 \times r \times Z_n^{7/2} Z_{\text{eff}}^{1/2} T^4, \quad (\text{III.14})$$

with  $Q_s$  in W/cm. This procedure gives the dash-dot line in Fig. 8.

Surfacelike radiation from this plasma is much weaker than blackbody emission. A blackbody cylinder of radius  $r$  radiates  $Q_{\text{BB}} = 2\pi r \sigma_{\text{SB}} T^4$  per unit length, where the Stefan-Boltzmann constant  $\sigma_{\text{SB}} = 10^5 \text{ W/cm}^2 \text{ eV}^4$ . This is the solid line in the left-top corner of Fig. 8(a), but off-scale in Fig. 8(b). The emissivity  $Q_s/Q_{\text{BB}} \simeq 4 \times 10^{-7} Z^{7/2}$  is about 1/30 for iron.

Estimating the opacity effects with a simple two-level model is highly approximate but still semiquantitatively correct. For example, a detailed radiation transport model with 162 levels and 511 radiation lines (Apruzese 1989/90) finds an emissivity below  $\sim 0.1$  for a krypton ( $Z_n = 36$ ) cylinder (with relevant plasma parameters  $n_e \sim 5 \times 10^{22}/\text{cm}^3$  and  $T = 1 \text{ keV}$ ). Figure 9 shows the x-ray spectrum for this computation. Many individual lines have merged together in two broad bands that approach the blackbody spectrum and account for most of the radiated energy. In this regime, around the transition from volume to surface radiation, the spectrum exceeds the blackbody limit for certain photon energies, reflecting the approximations even in this relatively comprehensive computation.

The different radial dependencies of radiation with the opacity effects and with Joule heating allow the determination of an equilibrium radius  $r_{\text{eq}}$ . Figure 8 shows the radial dependence of Joule heating in the double solid line, and the intersection with  $Q(r)$  that gives the equilibrium radius  $R_{\text{eq}}$ . The equilibrium radius decreases with increas-

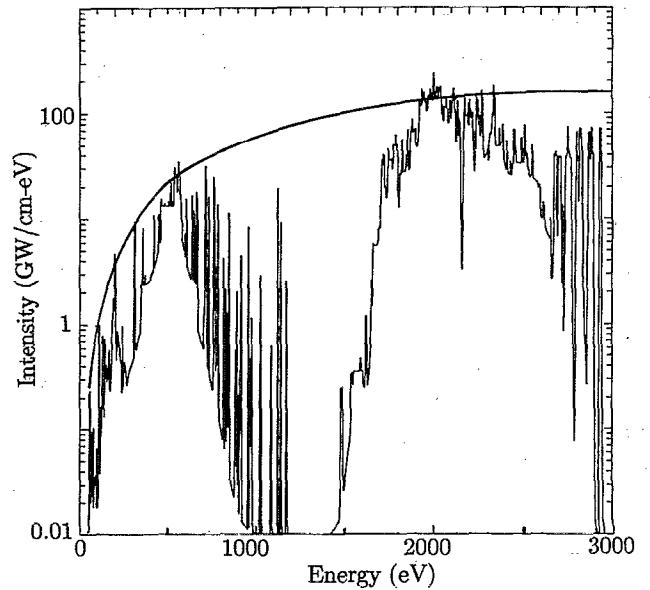


FIG. 9. Computed spectrum from a cylindrical krypton plasma of 0.01 cm radius, ion density  $4.9 \times 10^{22}/\text{cm}^3$ , and temperature 1 keV. Spectrum exceeding Planck limit in two regions indicates breakdown of approximation technique (from Apruzese 1989).

ing temperature, from about  $6 \mu\text{m}$  for 700 eV iron to about  $1 \mu\text{m}$  for 1700 eV iron. Such behavior has a clear physical reason. The higher temperature plasma is more coronal, and at the same time the radiated photons are more energetic and the absorption coefficients are lower. Therefore a higher compression is needed to reach the surfacelike radiation regime.

Using the analytical approximation for surfacelike radiation  $Q_s$  [Eq. (III.14)], and for Joule heating [Eq. (III.3)] gives an analytical estimate for the equilibrium radius,

$$r_{\text{eq}} \simeq 10^4 \left( \frac{I^2 Z_{\text{eff}}^{1/2}}{T^{11/2} Z_n^{7/2}} \right)^{1/3}, \quad (\text{III.15})$$

where  $r_{\text{eq}}$  is in cm.

These considerations are valid only if the current is larger than the critical current  $I_{\text{cr}}$  for which Joule heating would be balanced by volumelike radiation without opacity effects. As shown below III.10 the Joule heating increases with current as  $Q/l \propto I^2$ , but radiation increases faster, as  $Q_{\text{rad}} \propto I^4$ . Then Joule heating is less than volumelike radiation [as in Figs. 8(a) and 8(b)], and equilibrium is obtained with opacity-reduced radiation. In the opposite case  $I < I_{\text{cr}}$  Joule heating always exceeds radiation losses, and an equilibrium radius does not exist. The critical current  $I_{\text{cr}} \simeq 0.016 T^{3/4} Z_{\text{eff}}/Z_n^2$  increases with temperature: for an iron pinch  $I_e \simeq 0.2 \text{ MA}$  for  $T = 3 \text{ keV}$ .

The solid line in Fig. 10 shows the equilibrium radius for an iron plasma with current 0.2 MA, calculated according to Eq. (III.15), as a function of electron temperature. The lower scale is the ion density corresponding to Bennett equilibrium with a fixed current. The dashed curve shows the equilibrium radius  $r_{\text{eq}}$  calculated with an improved representation of  $W_d/W_r$ , that takes into account the transition

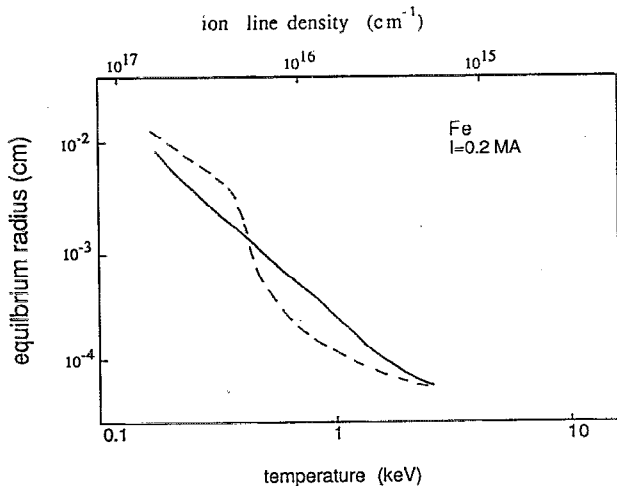


FIG. 10. Equilibrium radius for an iron at 0.2 MA vs temperature or linear ion density. The approximate power coefficient gives the solid line. Jacobs' power coefficient gives the dashed line.

from M shell (Ar-like) to L shell (Ne-like). This transition is responsible for the relatively rapid change in equilibrium radius  $r_{\text{eq}} \approx 10 \mu\text{m}$  around 0.4 keV. Nevertheless, the more elaborate result does not differ much from the rough analytical approximation, because the equilibrium radius is weakly dependent on the details of the radiation physics (about as the 1/3 power of the various coefficients). The equilibrium radius curve ends at the cross, at  $T = 3 \text{ keV}$ , where  $I_{\text{cr}} = 0.2 \text{ MA}$  and power equilibrium is no longer possible.

The analytical formula for  $r_{\text{eq}}$  combined with Bennett equilibrium gives an estimate for the electron density in the plasma, viz.,

$$n_{e,\text{eq}} \approx 10^{13} I^{2/3} Z_n^2 T^{8/3}, \quad (\text{III.16})$$

where  $n_{e,\text{eq}}$  is in  $/\text{cm}^3$ .

All these formulas were obtained considering only radiative losses and Joule heating with Spitzer conductivity with  $\ln \Lambda \sim 10$ . Other energy gain or loss mechanisms, such as anomalous resistivity or plasma outflow, give another value for the equilibrium radius, which is still defined by  $Q_{\text{Joule}} = Q_r$ . Vikhrev (1982a) considered  $r_{\text{eq}}$  including a model for anomalous resistivity from current-driven instabilities (see below).

### 3. Formation of a micropinch in a vacuum spark

The zero-dimensional equilibrium of the pinch estimated above is hydrodynamically unstable to the sausage instability ( $m = 0$ ). The radiative collapse model (Vikhrev 1982a) assumes that the hot spot in a low-inductance vacuum spark is caused by a local contraction due to the plasma outflow from the neck of the sausage, aided by large radiative energy losses. Such a development is visible in the experimental data of e.g., Veretennikov (1985), which shows a sausage-type instability in an iron pinch with current 0.15 MA, with a plasma radius in the neck around 0.01 cm and temperature of about 100–150 eV. These measurements agree with the estimates for the equi-

librium radius, which is also  $r_{\text{eq}} \sim 0.01 \text{ cm}$ . Other measurements support the existence of plasma outflow: an argon pinch shows a fourfold reduction of the initial line density, from  $6 \times 10^{16}/\text{cm}$  to  $\sim 1.5 \times 10^{16}/\text{cm}$  (Hares 1985); the axial velocity of the plasma increases with ionization states (Stewart 1987), and therefore with temperature.

In the radiative collapse model the outflow of particles along the pinch axis decreases the line density in the pinch region. However, during the outflow the pinch plasma remains in quasi-equilibrium, and the equilibrium radius and associated quantities change along the curve  $r_{\text{eq}}(N_i)$  shown in Fig. 10. An earlier model (Vikhrev 1977) assumed that the outflow of particles is the sole energy loss mechanism.

The decrease in the line density due to axial plasma loss is approximated by the equation:

$$\frac{dN_i}{dt} = -\frac{N_i}{\tau}, \quad (\text{III.17})$$

where  $\tau$  is a characteristic escape time. A reasonable value is  $\tau \approx h/c_s$ , where  $h$  is the height of the sausageing part of the pinch and  $c_s$  is the sound speed, or  $\tau \approx r/c_s \times \alpha$ , where  $\alpha$  is the aspect ratio of the sausage,  $\alpha = h/r$ . Typically,  $\alpha$  is in the range  $1 < \alpha < 10$ , or about 3.

Using the equilibrium values of radius [Eq. (III.15)] and density [Eq. (III.16)] with initial values for current  $I_0$  gives for the temperature

$$T(t) = \frac{T_0}{(1 - t/\tau_0)^{2/3}}. \quad (\text{III.18})$$

Here  $T_0$  is the initial temperature, and the characteristic timescale  $\tau_0$  is

$$\tau_0 \approx 0.006 \frac{\alpha I_0^{2/3}}{Z_n^{2/3} T_0^{5/3}}, \quad (\text{III.19})$$

with  $\tau_0$  in seconds. Equation (III.18) indicates that the temperature could increase rapidly after a time on the order of  $\tau_0$ . Radius and density will behave similarly, because these are directly coupled to the temperature  $T(t)$  by Eqs. (III.15) and (III.16).

The time constant  $\tau_0$  can be taken as the characteristic lifetime of the micropinch with initial parameters  $T_0$  and  $r_{\text{eq}}$ . For a low-inductance vacuum spark in iron with current  $I_0 = 0.2 \text{ MA}$  the lifetime of the plasma with aspect ratio  $\alpha = 3$  is  $\tau_0 \approx 14 \text{ ns}$  at temperature  $T \approx 100 \text{ eV}$ . This delay agrees reasonably well with the delay time between the initial compression to the equilibrium radius  $r = 0.01 \text{ cm}$  and the high-temperature micropinch stage with K-line radiation emission (Veretennikov 1981a,b). The calculated characteristic time for a plasma with temperature  $T \approx 1500 \text{ eV}$  when K ions radiate is about 20 ps, which also agrees with experimental measurements described above.

The radiative collapse model envisions a pinch in radiative equilibrium that produces a high temperature during a radiation-assisted compression with axial outflow of material. The high temperature ionizes the pinch ions to the K shell, and the pinch radiates K lines. During the compression the pinch remains in radiative equilibrium.

Radiative equilibrium demands that the current  $I_0$  remain less than the critical current  $I_{cr}$ , Eq. (III.9). However,  $I_{cr}$  increases with temperature as  $T^{3/4}$ . Eventually  $I_{cr}$  exceeds the pinch current  $I_0$ , which remains constant during the radiative collapse. At this point the pinch can no longer remain in radiative equilibrium. Once out of equilibrium the plasma expands, the density decreases, and the radiation stops.

K line radiation starts at a temperature  $T_K(Z_n)$  that depends on the nuclear charge  $Z_n$ . This happens approximately when  $T_K \approx 3 \times 10^{-3} Z_n^4$  eV (Breton 1978). The plasma point can radiate K lines if the critical current  $I_{cr}(T, Z_n)$  at  $T_K(Z_n)$  exceeds the pinch current  $I_0$ . Taking  $Z \approx Z_n \approx Z_{eff}$  gives the maximum atomic number for which the K shell can be reached:

$$Z_{max} \approx 70 \times I^{1/2}, \quad (III.20)$$

with  $I$  in MA. According to this formula He-like ions with  $Z_n \lesssim 30$  or so can be excited in a micropinch with  $I_0 = 0.2$  MA. This agrees with experiment: iron ( $Z_n = 26$ ) is stripped to the K shell in a micropinch with  $I_{max} \approx 0.2$  MA, while in a molybdenum ( $Z_n = 42$ ) pinch the K lines are very weak.

A similar estimate can be made for Ne-like ions. These appear when  $T_{Ne} \approx 5 \times 10^{-4} Z_n^4$ ; therefore, ions with nuclear charge  $Z_{max} \lesssim 135 \times I^{1/2}$  can be expected to radiate L lines. For a pinch with  $I_0 = 0.2$  MA the estimate,  $Z_{max}^N \lesssim 55$ , is in good agreement with experimental observations (Aglitskii 1986).

Another quantity of interest is the radial size of the plasma point seen in K line light, and the point's electron density. Equation (III.15) gives an equilibrium radius  $r_{eq} = 1 \mu\text{m}$  for an iron plasma at  $I = 0.15$  MA with temperature  $T = 1700\text{--}2000$  eV,  $r_{eq} = 5 \mu\text{m}$  for calcium ( $Z_n = 20$ ) at  $T = 100$  eV, and  $r_{eq} = 15 \mu\text{m}$  for sulphur ( $Z_n = 16$ ). These numbers compare favorably with the experimental observations in Fig. 1. There is also good agreement for the electron densities: for calcium  $n_e = 10^{23}/\text{cm}^3$  under the circumstances given, and for aluminum ( $Z_n = 13$ )  $n_e = 4 \times 10^{21}/\text{cm}^3$  at  $T = 400$  eV.

The radiation power of the plasma point is obtained by multiplying the surface-like radiation power per unit length (III.14) by the micropinch length ( $\alpha \times r_{eq}$ ). This gives for the radiation power of the plasma point the expression

$$Q_{tot} = 2.7\alpha \times I^{3/4} Z_n^{7/6} Z_{eff}^{5/6} T^{1/3}, \quad (III.21a)$$

with  $Q_{tot}$  in MW. With the usual approximations  $h\nu \approx 2kT$  and  $Z_n \approx Z_{eff}$  this becomes

$$Q_{tot} \approx 2.1\alpha I^{4/3} Z_n^2 (h\nu)^{1/3}, \quad (III.21b)$$

which shows a weak (1/3 power) dependence on photon energy  $h\nu$ . For an iron plasma with  $\alpha = 6$  and  $I = 0.15$  MA the power radiated by the plasma point varies from  $Q_{tot} = 3$  GW for a choice of  $h\nu = 0.2$  keV, to 10 GW for  $h\nu = 6$  keV.

The total energy  $\epsilon$  radiated by the point in the region between  $h\nu$  and  $1.5 h\nu$  can be estimated multiplying the power  $Q_{tot}$  by the lifetime  $\tau$ :

$$\epsilon \approx 7 \times 10^4 \alpha^2 I^2 Z_n^{4/3} / (h\nu)^{13/6}. \quad (III.22)$$

This estimate gives  $\epsilon \approx 0.02$  J for the K-radiation from a plasma point in an iron plasma. The experimental value is also 0.02 J. Obviously, this exact coincidence is accidental: both theory and experiment are only accurate to within a factor of 2.

Below we discuss the results for a more accurate numerical model of micropinching. However, the simple physical investigation above already suggests that the model of radiative compression correctly describes qualitatively and quantitatively many aspects of the physical scaling of plasma points.

### C. Zero-dimensional dynamic model of micropinching

The zero-dimensional dynamic model of micropinching (Vikhrev 1982a) discussed below is the first qualitatively and quantitatively correct description of many of the characteristics of plasma points. This model grew out of the so-called simple model of the plasma focus by adding radiative energy losses due to line radiation of multiply charged ions. It gives good results for an iron pinch, which has been studied in detail.

In the final stage of the hydromagnetic sausage instability the pinch evolves into a neck with an elongated shape, with height  $h$  and radius  $a$  (Böök 1976). The aspect ratio  $\alpha = h/a$ , and  $\alpha \sim 3\text{--}10$ . The center of the neck is at  $z = 0$ , and the neck edges are at  $\pm h/2$ . Density and temperature are taken to be uniform throughout the neck. During compression the uniformity is maintained when the radial speed  $v_r(r) = (r/a)v$  is linear with radius:  $v = v_r(a)$  is the radial velocity at the column edge.

What is the compression dynamics of the neck? Radial motion follows the equation:

$$\frac{2}{3} mn \frac{dv}{dt} = -2\pi a \left( p - \frac{2nT}{\pi a^2} \right). \quad (III.23)$$

Here  $m$  is the ion mass and  $p = B^2/2\mu_0$  is the magnetic pressure at the plasma edge. The change in the line density  $N = \pi a^2 n$  is given by

$$\frac{dN}{dt} = -\frac{N}{\tau}. \quad (III.24)$$

The constant  $\tau$  is the characteristic escape time of the plasma:

$$\frac{1}{\tau} = \frac{1}{\tau_z} + \frac{1}{\tau_r}, \quad (III.25)$$

where  $\tau_z$  is the escape time of the plasma through the ends of the plasma column, and  $\tau_r$  is the radial compression time. It is given by the growth rate of the hydromagnetic instability corrected with the aspect ratio  $\alpha$ , viz.,  $\tau_r = \alpha(a/c_s)$ , where  $c_s$  is the Alfvén speed (and the ion thermal speed in Bennett equilibrium,  $v_{Ti}$ ).

The velocity of the plasma along the  $z$  axis at the edge of the neck determines the axial escape time  $\tau_z = h/2v_z$ , where the axial velocity  $v_z$  is given by

$$\frac{dv_z}{dt} = \frac{2}{hnm} \frac{(nT - n_0T_0)}{h/2} - \frac{v_z^2 h}{h/2}. \quad (\text{III.26})$$

Here  $n_0$  and  $T_0$  are the density and temperature of the plasma escaping from the pinch. The first term on the right hand side contains the pressure gradient along the  $z$  axis. The second term describes the decrease of  $v_z$  due to the escape of plasma through the ends, under the assumption that the axial velocity increases linearly with axial distance  $z$ .

The energy per unit length of the plasma column is  $\epsilon N_b$ , with  $\epsilon$  the average energy per ion. The energy per unit length develops according to the equation:

$$\frac{d(\epsilon N_b)}{dt} = -2\pi ap \frac{da}{dt} - \frac{\epsilon N_b + \pi a^2 p}{\tau} - Q. \quad (\text{III.27})$$

The first term on the right hand side is the power input by adiabatic compression, and the second describes the outflow of energy associated with the escape of material from the neck. The last term is the radiation loss.

The pinch current is given by the circuit equation:

$$\frac{d}{dt}[(L_0 + L_p)I] + R_p I = 0, \quad (\text{III.28})$$

where  $L_0$  and  $L_p$  are the inductances of the circuit and the discharge channel, respectively, and  $R_p$  is the resistance of the neck region in the plasma.

The resistance  $R_p = h/\sigma\pi a^2$ , with  $\sigma$  the plasma conductivity. To mock up anomalous resistivity the conductivity  $\sigma$  is taken to be  $\sigma = nev/mv_{\text{eff}}$ , with  $v_{\text{eff}} = v_{ei} + v_{\text{anom}}$  the effective collision frequency. Spitzer conductivity comes from elastic collisions between electrons and ions, with collision frequency  $v_{ei}$ . The collision frequency  $v_{\text{anom}}$  takes into account an anomalous resistivity related to plasma instabilities that may be excited by current flow in the pinch. In the absence of a good model the anomalous collision frequency is taken as

$$v_{\text{anom}} = (v_D/v_{Ti})^2 (\omega_{ci}/\omega_{ce})^{1/2}. \quad (\text{III.29})$$

Here  $v_D$  is the drift velocity of the electrons, and the  $\omega_c$ 's are the ion and electron Larmor frequencies. The formula primarily serves to define a reasonable timescale for a typical but unspecified current-driven instability in a strong magnetic field. The important point here is to include an anomalous resistivity effect: further research is needed to pin down the appropriate instability, and to replace Eq. (III.29) with an updated formula. At this time it is sufficient that an instability threshold is reached (at constant current) when the plasma escapes from the neck, the line density  $N$  decreases, and the drift velocity  $v_D \sim I_0/N$  exceeds the thermal velocity.

The computation shown below (Ivanov 1986) includes the anomalous resistivity, and a slightly more elaborate way of computing radiative loss than described here, viz., various line broadening effects for calculating the optical depths of individual lines. These added features allow the study of fine detail in the compression of micropinches, but the simple approach for calculating radiative losses is quantitatively correct for the basic properties.

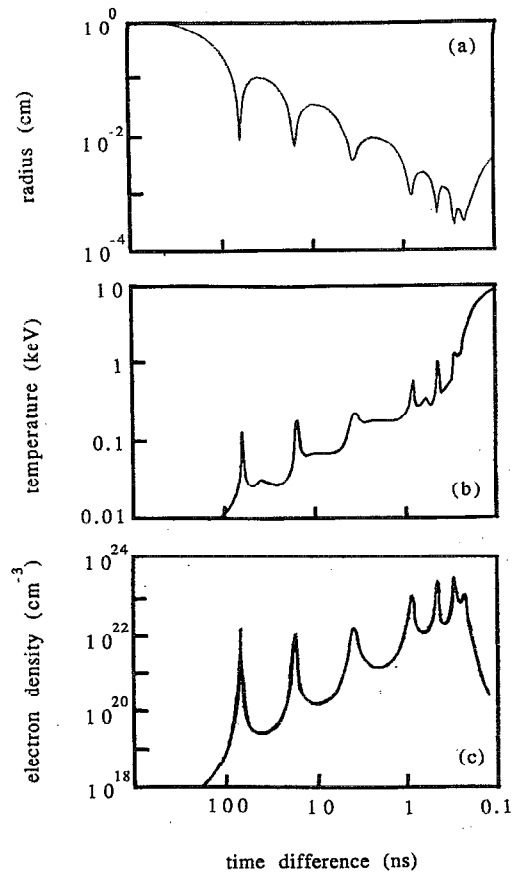


FIG. 11. Zero-dimensional numerical modeling of micropinching in an iron plasma with peak current  $\sim 150$  kA: (a) plasma radius; (b) electron temperature; (c) electron density.

Figure 11 shows the temporal evolution of the plasma parameters during the process of micropinching. A special logarithmic time difference scale is used to represent all stages in a single graph. Zero time is the end of the final compression, usually when the temperature exceeds some high, but arbitrary value (20–50 keV). The duration of any stage corresponds to the difference between the ordinates.

The initial conditions for this computation are given on top of the figure. The distance between the iron electrodes is equal to the initial radius of the plasma, 1 cm, and an initial line density is  $N_i = 3 \times 10^{17}/\text{cm}$ . The first regime is a slow compression during the first 920 ns or so, followed by an hydrodynamic series of compressions and expansions (similar to Felber 1982) topped off by a fast radiative collapse in the final 1 ns.

At first the plasma compresses hydrodynamically to a radius 70–80  $\mu\text{m}$ , at  $\sim 90$  ns before the end of the computation, expands, and compresses again to a radius that decreases with each subsequent compression due to radiative energy loss (Meierovich 1985). These compressions end with a very small plasma region reminiscent of a plasma point, with radius around 3  $\mu\text{m}$ . The temperature in Fig. 11(b) gets into the region 1–10 keV at this stage. The electron density in Fig. 11(c) goes up to  $n_e \simeq 10^{23}/\text{cm}^3$ .

In this computation the plasma is initially uniform over radius. In this case the formation time of the plasma

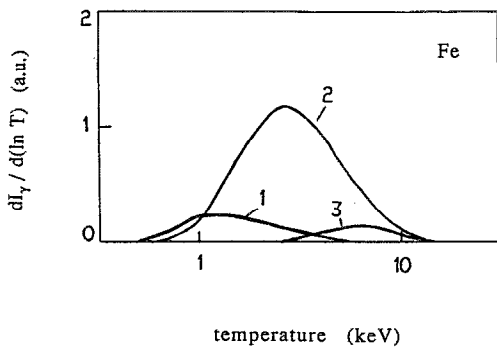


FIG. 12. Intensities of radiation versus temperature for iron: (1) dielectronic satellites of Li-like ions; (2) resonance lines of He-like ions; (3) resonance lines of H-like ions.

point, taken from the second compression to the end of the run, is about 20 ns. In other runs, where different radial distributions are assumed, the formation time varies from 50 to 20 ns. These values agree well with observations of the dynamics of micropinching.

The stagnation phase, between 20 and 1 ns, is characterized by a plasma radius  $r \approx 0.1\text{--}0.2$  mm, electron temperature  $T \approx 100$  eV, and an electron density oscillating around  $n_e \sim 10^{21}/\text{cm}^3$ . These parameters agree reasonably well with observations of the plasma during hydromagnetic compression.

In the plasma point region [denoted by "K" in the Fig. 12(a)], the plasma contracts to a radius of order  $3 \mu\text{m}$ . The electron density in this compression stage varies from  $n_e \sim 3 \times 10^{23}/\text{cm}^3$  to  $n_e \sim (1\text{--}2) \times 10^{24}/\text{cm}^3$ ; the electron temperature increases from 1.3 to 5 keV. The lifetime of the plasma point with radius  $r < 2 \mu\text{m}$  is shorter than 100 ps. The calculated lifetime of the hot phase of the micropinch agrees well with the measured values (Agliitskii 1985) of 20 ps.

After the final compression the plasma column expands rapidly due to the fast loss of plasma from the pinch and the simultaneous appearance of anomalous resistance. During the expansion the plasma temperature continues to increase rapidly, reaching tens and more of keV. However, the expansion phase does not contribute significantly to K-line radiation due to its short lifetime and the rapidly decreasing plasma density.

Figure 11 appears to contain the basic phenomena observed in micropinching, including quantitatively correct results for the plasma parameters of the plasma point. The model also gives a quantitatively reasonable account of the plasma point's disassembly. We conclude that the radiation compression model captures the principal physics of radiation collapse. In the next section we discuss the scaling of plasma point parameters with initial parameters such as nuclear charge  $Z_n$ , peak current, and initial line density.

#### IV. EXPERIMENTAL RESULTS ON PLASMA POINTS INTERPRETED WITH THE RADIATION COLLAPSE MODEL

Section II presented the experimental results on plasma points, and Sec. III gave a computation for radia-

tion collapse of an iron pinch. This section uses the radiation collapse computation to interpret the experimental results. An important insight is that in a radiative collapse the plasma goes through a wide range of temperatures. As a result, the different measurement techniques for the electron temperature all give values within their range of validity. Electron temperature measurements for plasmas of various compositions corroborate the radiation collapse scenario. Radiative collapse can evolve in two different types of plasma points.

##### A. Electron temperature of plasma points

Computations of radiative collapse suggest that the plasma point goes through two orders of magnitude in density and temperature in a sub-ns time. In contrast, the x-ray spectral measurements are time-integrated, while their interpretation in terms of density and temperature usually assumes a stationary plasma. The plasma parameters obtained this way are always somewhere in the sensitivity range of the particular measurement technique. Measurements valid in widely different regimes then give widely different results corresponding to the regimes of validity.

Consider first the procedure for measuring the electron temperature  $T_e$  by the relative intensities of dielectronic satellites to the H- and He-like resonance lines. Figure 12 gives the relative intensity  $I_r$  for the resonance lines of H- and He-like iron ions, and for the dielectronic satellite lines, as function of temperature  $T$ . The intensities are given as  $dI_r/d(\log T)$  to compensate for the logarithmic temperature scale, so that the total radiation in a specific line is proportional to the area under the corresponding curve. The intensities come from the iron pinch computations of Ivanov (1986), and take into account the changes in radius and density of the plasma point during its evolution over the last 200 ps of its life (see Fig. 11). Although the intensities vary with time it is possible to plot them as function of temperature, because the temperature increases monotonically with time.

Singly excited He-like iron is most abundant at a temperature of  $T_e \approx 2.5$  keV, and therefore the resonance line of He-like iron is strongest at this temperature. For the same reason the resonance line of H-like iron peaks at a higher temperature  $T_e \approx 6$  keV. Excitation of Li-like iron accounts for the satellites of the He-like resonance line, which therefore peaks at the lowest temperature  $T_e \approx 1$  keV.

A spectrometer does not see the intensity ratios at each particular temperature if it is slow compared to the 20 ps timescale of plasma point formation. Instead, it registers the time-integrated intensity. The ratio between the time-integrated intensities corresponds to some intensity ratio for instantaneous intensities. The intensities of the H- and He-like resonance lines can be used to measure the temperature between 2.5 and 8 keV. Therefore, the effective temperature inferred from a time-integrated measurement with these lines,  $T_{\text{He/H}}^{\text{eff}}$  is some average value, here  $T_{\text{He/H}}^{\text{eff}} \approx 3.8$  keV, which depends somewhat on the detailed time history of the plasma point. Likewise, the effective

temperature  $T_{\text{He-DS}}^{\text{eff}} \approx 1.9$  keV obtained from the ratio of dielectronic satellites to the He-like resonance line lies in the region where this temperature measurement is applicable. When the plasma point's temperature traverses a wide range of temperatures the measurement technique gives some arbitrary temperature in the regime of validity.

Similar arguments apply for temperature measurements with bremsstrahlung. In an optically thin plasma with temperature  $T_e$  the spectral intensity  $I(h\nu)$  in harder photons with  $h\nu \gg kT_e$  varies exponentially with photon energy  $h\nu$ . The temperature defined by this continuous spectrum is then  $kT_e = -d(h\nu)/d[\ln I(h\nu)]$ , which depends on the length of time that the plasma point spends in the photon energy regime used for the measurement. Therefore this approach produces temperatures that increase with the hardness of the radiation used for the measurement (Lee 1974; Burhenn 1984), and that are higher than the temperatures deduced from the line ratios. The computation of radiation collapse shows that the effective temperature in the micropinch would be  $T_{30}^{\text{eff}} \approx 7$  keV when measured in the energy band around  $h\nu \approx 30$  keV, but would increase to  $T_{100}^{\text{eff}} \approx 11$  keV for the energy band  $h\nu \approx 100$  keV.

Other computations show that the temperature inferred from bremsstrahlung varies with pinch current in a qualitatively correct manner. Changing the current from 100 to 150 kA increases the temperature in the computations from 9 to 11 keV (measured with radiation around  $h\nu \approx 50$  keV). Under similar circumstances in an experiment the temperature of the plasma point increases from 5 to 7 keV (Bykovskii 1982).

## B. Experiments with compound plasmas: Fe/Mo, Ti/Mo, Ti/Nb

The radiative collapse model predicts that density and temperature of plasma points increase with the atomic number of the element used in the pinch. Unfortunately, time-integrated measurements on the same line for the different elements also give results that increase with increasing atomic number. This problem is resolved by using a single element selected for diagnostic purposes intermixed with heavier elements.

Plasma parameters were inferred from the spectra of He-like iron Fe xxv in a pure iron pinch and a mixed iron-molybdenum pinch (Vikhrev 1982b; Sidel'nikov 1982b). Figure 13(a) is the spectrum from 100 discharges with pure iron, Fig. 13(b) from an iron-molybdenum pinch, with 50% Mo ( $Z_n = 42$ ).

The spectra can be fully interpreted with the spectrum fitting procedure discussed earlier, but some qualitative features are obvious. The shape of the long-wavelength wing of the "j" satellite is equally broad in both spectra, and not through accidental overlap with other lines. Thus individual lines in both spectra have the same intrinsic broadening. However, the measured width of the resonance line is due to the overlap with the dielectronic satellites with principal quantum number  $n > 3$ . This width is  $4.2 \times 10^{-3}$  Å for Fe, but decreases to  $3.4 \times 10^{-3}$  Å for (Fe + Mo), reflecting a smaller contribution of the satel-

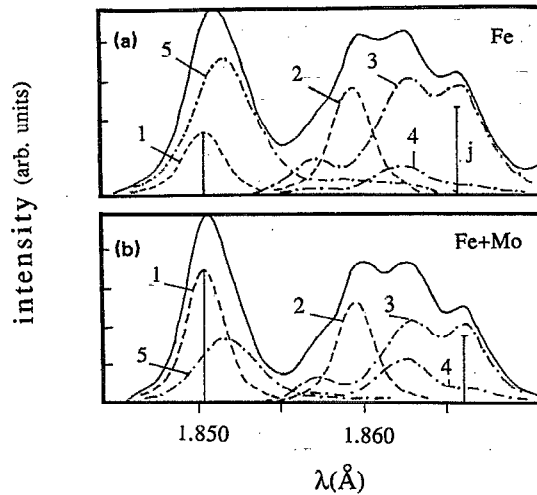


FIG. 13. Spectrum of a plasma point (a) with an anode of pure iron; (b) with a 50% iron, 50% molybdenum anode.

lites to the long-wavelength wing of the total lineshape due to the increased temperature of the emitting plasma.

The full fitting procedure shows that the relative intensity of dielectronic satellites in the (Fe + Mo) plasma is 3–3.5 times smaller than the pure iron plasma. The intensity decrease corresponds to an increase in the electron temperature from 1.4 keV for pure iron to 2.0–2.4 keV for the compound (Fe + Mo) plasma.

The spectrum around the resonance line of Fe xxv can not be used to measure the plasma's electron density using the collisional mixing of autoionized states, but this can be done with spectra of Ti xx–xxi. Therefore, titanium plasmas with various admixtures were diagnosed by using the resonance line Ti XXI and its satellites (Sidel'nikov 1982b). The electrodes in these experiments varied from pure titanium to a blend of titanium with 20%–50% of molybdenum and niobium ( $Z_n = 41$ ).

The measurements are not precise enough to see a difference in the spectrum with a 20% admixture of Mo and Nb to the titanium, but a 50% admixture of heavy impurities (Mo or Nb) gives a  $\sim 20\%$  narrower resonance line due to a smaller contribution from the intercombination and dielectronic satellite lines. Full analysis of the spectra shows that the temperature increases  $T_e$  from 1.2–1.3 keV for a pure Ti pinch to  $T_e \approx 1.4$ –1.5 keV for Ti with a 50% admixture of heavy impurities. The increase in the density-sensitive satellite "q" corresponds to an increase in the electron density by a factor of about 1.5. These careful estimates of density and temperature for plasma points with different atomic numbers confirm the expectations from the radiative collapse model: time-averaged diagnostics give values for density and temperature that increase with atomic number.

## C. Two regimes of micropinching

Many experiments integrate x-ray spectra over many shots under the assumption that all plasma points are similar in character. However, plasma points do not develop

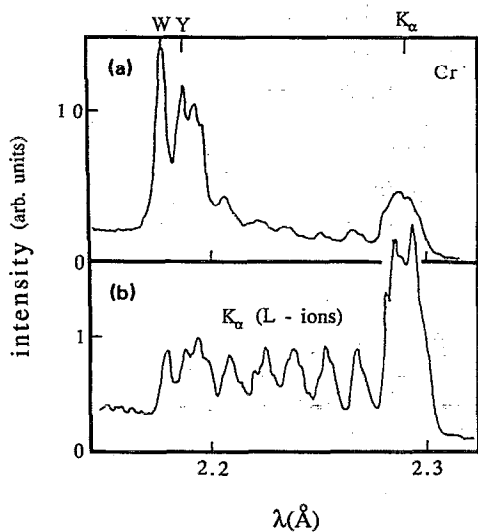


FIG. 14. Spectrum in chromium ( $Z_n = 24$ ): (a) from a small plasma point ( $d < 3 \mu\text{m}$ ); (b) from a large plasma point ( $d \approx 100 \mu\text{m}$ ).

on some shots, and when a plasma point appears it can have quite irreproducible size and position. What happens in individual plasma points?

Single-shot spectra must be studied with a highly sensitive spectrometer (e.g., Schultz 1989; Aglitskii 1984). The measurement technique (Antsiferov 1989) uses a curved quartz crystal spectrograph with different crystals ( $2d = 2.26, 4.91, \text{ and } 6.68 \text{ \AA}$ ) and radii of curvature  $R = 300\text{--}800 \text{ mm}$ . The spectra are amplified by a micro-channel plate covered by a layer of ZnS doped with Ag (Aglitskii 1984), and registered photographically. Plasma size can be correlated with the spectrum on each shot by using the blurring of the x-ray image's edge.

These measurements, done with a maximum current  $I_m \sim 150\text{--}200 \text{ kA}$  and plasmas of Cr, Mn, and Fe, give two types of plasma points, large and small. The small plasma points are a few  $\mu\text{m}$  across, the large plasma points are  $\sim 0.1 \text{ mm}$  in diameter. Both types, large and small, emit spectra with resonance lines ( $1s^2 - 1s2p^1P_1$ ) and intercombination lines ( $1s^2 - 1s2p^3P_1$ ), and also satellite transitions in ions of low multiplicity, but obvious differences in the spectra suggest that the plasma points have quite different parameters.

The chromium (Cr,  $Z_n = 24$ ) spectra in Fig. 14 are good examples. Figure 14(a) is a spectrum for a small plasma point, and Fig. 14(b) for a large plasma point. The spectra contain the same lines, but in quite different proportions: the small plasma point radiates  $\sim 10\times$  more in the resonance line (line "W" at  $2.19 \text{ \AA}$ ), and the satellite transitions are relatively less important. In the large plasma point [Fig. 14(b)] the dominant radiation consists of  $K_\alpha$  lines, between  $2.1$  and  $2.9 \text{ \AA}$ , probably excited by nonthermal electrons of a colder plasma in the L-shell ionization state. The nonthermal electrons could be isotropic, but they are more likely in the form of a directed beam: the spectrum is consistent with both possibilities.

Plasma of lighter elements, such as sulphur

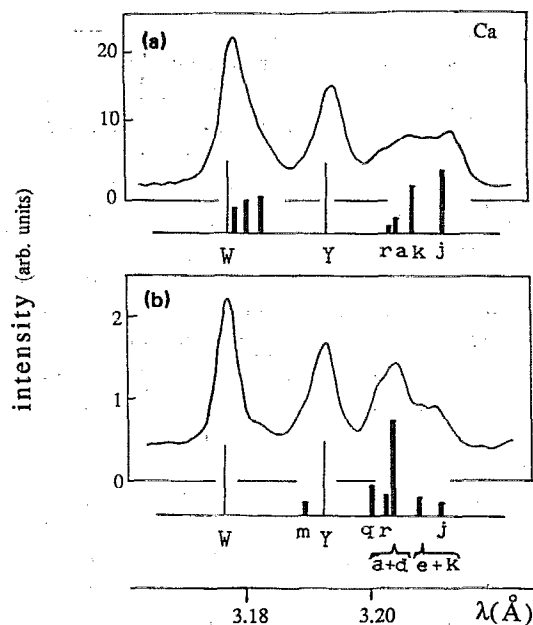


FIG. 15. Spectrum in a calcium ( $Z_n = 20$ ) plasma: (a) from a small plasma point; (b) from a large plasma point. The bars give the positions and relative magnitudes of the brightest dielectronic satellites.

( $Z_n = 16$ ) and calcium (Ca,  $Z_n = 20$ ), show analogous results, but now the diameter of the small plasma point is about  $10\text{--}15 \mu\text{m}$ , while the large plasma point is  $0.2\text{--}0.3 \text{ mm}$  across. Both regimes of micropinching were also found (Aglitskii 1986) for heavier elements, Cu at  $Z_n = 29$  and Zn at  $Z_n = 30$ . In this case the small points were smaller than the experimental resolution ( $< 3 \mu\text{m}$ ), while the large plasma points have diameters  $\sim 30\text{--}50 \mu\text{m}$ . The x-ray spectra of these elements show the same tendencies as in Fig. 14, so that for the large plasma points the resonance lines are practically absent.

A characteristic feature of the x-ray spectra from the large plasma points are dielectronic satellites excited from Li-like ions by electron-ion collisions, while the satellite lines in the x-ray spectra of the small plasma points come from dielectronic recombination. An example is the spectrum for a small plasma point in calcium, Fig. 15(a), compared to Fig. 15(b) for a large plasma point. The resonance line "W" for the small plasma point is visibly wider than the same line for the large plasma point, indicating dielectronic recombination due to the high density (compare the discussion of Fig. 13). The bars in Fig. 15 are the (relative) strengths of the different lines needed to fit the spectrum. These agree with predictions from dielectronic capture. The resonance line in the large plasma point is not broadened by satellites, and the relative strength corresponds to collisional excitation.

Why are there two kinds of plasma points? In the radiative collapse model the plasma point disassembles due to anomalous Joule heating connected with the development of microturbulence. If the plasma remains in the Joule heating regime during compression a small plasma point emerges, while a large plasma point is formed if

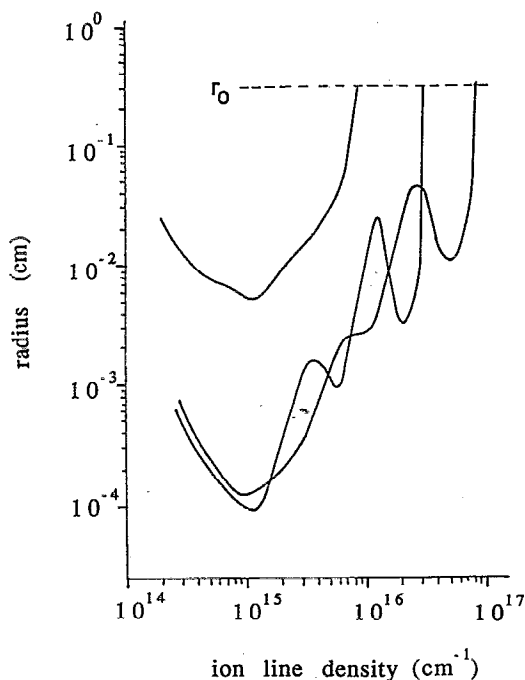


FIG. 16. Micropinching in iron for three linear ion densities  $N_i(r_0)$  and the same initial radius  $r_0 = 3$  mm.

anomalous heating exceeds the radiative losses early on in the compression process. Anomalous heating starts when the drift velocity  $v_D = I/eN_e$  is on the order of a characteristic thermal velocity in the plasma such as the ion sound velocity  $v_s = \sqrt{kT/M_i}$ . For a Bennett pinch  $v_D = v_s$  implies  $N_e r_e = M_i/m$ , where  $r_e = (e^2/mc^2)[1/4\pi\epsilon_0]$  is the classical radius of the electron. The critical line density would then be  $N_e \approx 3M_i/m \times 10^{12}/\text{cm}$ , corresponding to an initial line density  $N_0 \sim 10^{16}/\text{cm}$ , weakly dependent on the other pinch parameters such as temperature or the effective atomic number  $Z_{\text{eff}}$ .

According to these considerations the dynamics of micropinching may depend significantly on the initial line density in the discharge. The initial line density in a vacuum spark arises primarily as a result of evaporation of the anode by electrons pulled out of the pre-cathode plasma by the initial voltage. This complicated process is likely to give different initial line densities from shot to shot. Moreover, the line density of this plasma decreases with increasing distance from the anode, creating different initial conditions for the development of the pinch along the axis of the discharge.

The radiative collapse model is sensitive to the initial line density  $N_0$ . Figure 16 contains results from three computations on an iron plasma with 150 kA peak current and initial radius  $r_0 = 3$  mm, and different line densities given in the figure (Antsiferov 1989). Shown is the compression dynamics by plotting the radius  $r(t)$  and ion line density  $N_i(t)$  in the  $(r, N_i)$  plane.

In the initial stage of the compression the line density remains constant for all three cases, indicating no outflow of plasma. After this initial stage the tenuous case with  $N_i(0) = 10^{16}/\text{cm}$  loses mass while contracting radially un-

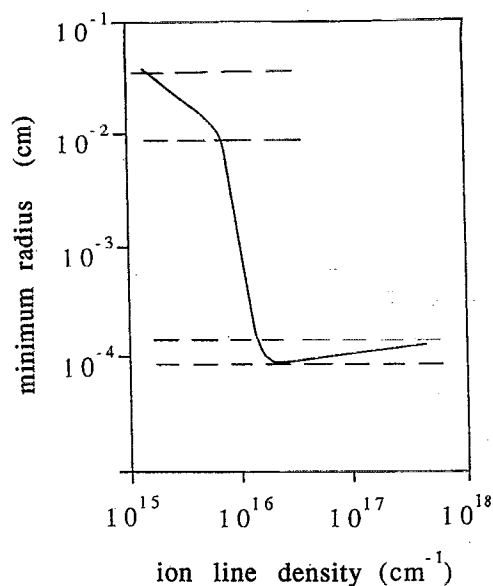


FIG. 17. The minimum radius of an iron plasma during micropinching as function of the initial linear ion density  $N_i$ .

til it reaches a minimum of 0.1 mm at  $N_i \approx 10^{15}/\text{cm}$ . In contrast, the pinches with initial line density  $\approx 2.5 \times 10^{16}/\text{cm}$  contract in an oscillatory fashion also seen in Fig. 11 (for different initial conditions). The final size is now much smaller,  $r_{\text{min}} \sim 1 \mu\text{m}$ . Expansion starts at about the same line density for all three cases, namely when the drift speed for the 150 kA current exceeds a thermal velocity.

Figure 17 shows the minimum radius  $r_{\text{min}}$  obtained during the compression as function of the initial line density. For initial line density  $N_i(0) > 10^{16}/\text{cm}$  the pinch reaches a minimum radius of 1–2  $\mu\text{m}$ , while for an initial line density  $N_i(0) < 10^{16}/\text{cm}$  the final pinch size exceeds  $\sim 0.1$  mm. The plot suggests two radiative collapse regimes, one with large final radius for pinches with small line density, and one with small final radius for more massive pinches, with a small transition region in between. A collapse with large final radius is reminiscent of the large plasma point, while the collapse with small final radius looks like a small plasma point. This phenomenology is corroborated by experimental data (Koloshnikov 1985): for aluminum the transition occurs around  $3 \times 10^{15}/\text{cm}$  (Ivanenkov 1989).

Other computations, for calcium ( $Z_n = 20$ ) and zinc ( $Z_n = 30$ ), show the same well-defined transition between the two micropinch regimes. Moreover, in these computations the minimum radius decreases with increasing nuclear charge  $Z_n$ , in agreement with experimental results.

The computed radiation output per plasma point agrees with the experimental value. In the computations the energy  $K$  lines from a small plasma point is about 0.04 J per shot, while the experimental value is about 0.02 J (Veretennikov 1985). For the large plasma point the computed K-line energy per shot is more than an order of

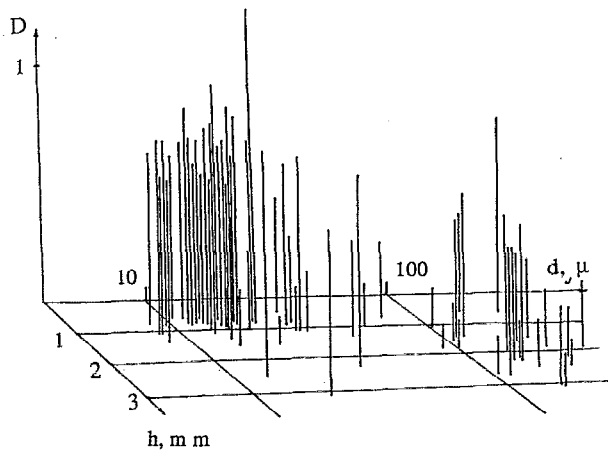


FIG. 18. Correlation between the size of  $d$  of the plasma point (horizontal axis), the distance between the anode and the point's  $h$  in the discharge gap (forward axis), and the intensity of radiation  $D$  (vertical axis). The plasma is titanium ( $Z_n = 22$ ), and the current is 100 kA.

magnitude less, in agreement with experimental data of Figs. 14 and 15.

The size of the plasma point is correlated with its position in the discharge gap (Antsiferov 1989) in a manner that is consistent with the two regimes of radiative collapse. The measurements were made at 100 kA in a Ti plasma ( $Z_n = 22$ ), with an experimental resolution of the pinch size of  $5 \mu\text{m}$ . Figure 18 shows the results. The forward pointing axis is the distance to the anode, the horizontal axis is the size of the plasma point, and the vertical axis is the intensity of the  $K$ -line output as gauged by the film density.

The data show two groups of plasma points. The small plasma points, with radius  $r \sim 10 \mu\text{m}$ , are located mainly close to the anode, while the large plasma points, with radius  $r \sim 0.2 \text{ mm}$ , are typically farther away. Moreover, the film density of the small plasma points is several times larger than for the large plasma points. These experimental data are consistent with the results in Figs. 16 and 17 obtained from computations on simple theoretical models.

## V. CONCLUSION

The experimental results appear to show a radiative collapse phenomenon in low-inductance vacuum sparks. Two types of plasma points have been documented, small plasma points around a few microns in size, with extreme values for density  $n \sim 10^{23}/\text{cm}^3$  and temperature  $T_e \gtrsim \text{keV}$ , and large plasma points with one order of magnitude larger size and two order of magnitude smaller density. Discrepancies between the values given in the literature over the years are explained in part by the two different regimes, and in part by the fact that a plasma point is dynamic: the plasma's density and temperature can change drastically during collapse. In this case the plasma parameters inferred from time-averaged x-ray spectroscopy depend on the range of validity of the measurement technique.

Many characteristics of the plasma points are successfully reproduced by a radiative collapse model (Vikhrev

1982a). The model's principal ingredients are the strong radiative power from the ions as modified by opacity effects, and the reduction of line density due to axial outflow. Radiative collapse ends by the onset of anomalous heating.

Other types of discharges with axial symmetry often show small, bright regions of x-ray emission that appear to be similar to the plasma points discussed here. For example, plasma points appear in experiments with exploding wires (Burkhalter 1977; Zakharov 1983). For currents up to 200 kA the parameters of the plasma point are close to the ones measured in low-inductance vacuum sparks.

Gas puff z-pinches also show plasma points, generally called bright spots in the z-pinch literature, whose size, temperature, and density of plasma appear to vary considerably depending on the type of the apparatus, the current in the discharge, and the initial conditions. However, it is possible to have a regime that produces small plasma points with sizes of several  $\mu\text{m}$  in a  $\sim 1 \text{ MA}$  current discharge (Gol'ts 1986/7; Sopkin 1990). The x-ray spectrum of the He-like krypton and xenon in these experiments shows plasma points with temperatures of tens of keV, and  $n_e \tau \gtrsim 10^{12} \text{ cm}^3/\text{s}$ .

Similar observations come from plasma focus experiments. Plasma points with size  $\sim 10 \mu\text{m}$  arise in the second compression of the focus, when the hydrogen plasma increases its radiation loss through additional anode material (copper) (Fillipov 1983). Similar phenomena are seen in experiments on a plasma focus discharge in a mixture of deuterium and heavy noble gases (Peacock 1969; Volobuev 1988; Koshelev 1988). The x-ray spectra of the heavy impurities indicate that the electron temperature reaches about 700–1000 eV in plasma points of about  $20 \mu\text{m}$ .

The addition of several percent impurities produces a significant change in the character of the final pinch in these and other experiments. In the explosion of  $\text{CD}_2$  wires (Young 1977) the radiation from carbon ions apparently leads to small plasma points (Decker 1990). Also the compression of z pinches in deuterium changes drastically with the admixture of high atomic number elements (Bailey 1986). These experiments again demonstrate the essential role of radiation loss on the dynamics of many types of discharges, and especially on plasma point formation.

Micropinches are primarily used as radiation sources for spectra of multiply charged ions, but in the future micropinches may become sources of XUV and soft x rays for technological applications (e.g., Veretennikov 1982), and for pumping of x-ray lasers (e.g., Finkenthal 1986; Oraevskii 1987). For this application it is important that the short lifetime of a micropinch corresponds to a high radiation power despite the small total energy.

- E. V. Aglitskii, E. Ya. Golts, Yu. A. Levykin, and A. M. Livshits (1984). *Opt. Spectrosc.* **56**, 33 (*Opt. Spectrosc.* **56**, 20).  
 E. V. Aglitskii, P. S. Antsiferov, and A. M. Panin (1985). *Fiz. Plazmy* **11**, 1266 [*Sov. J. Plasma Phys.* **10**, 726].  
 E. V. Aglitskii, P. S. Antsiferov, K. N. Koshelev, and A. M. Panin (1986). *Fiz. Plazmy* **12**, 1189 (*Sov. J. Plasma Phys.* **12**, 683).  
 S. G. Alikhanov, V. I. Vasilev, E. Ya. Kononov, K. N. Koshelev, Yu. V. Sidel'nikov, and D. A. Toporkov (1984). *Fiz. Plazmy* **10**, 1051 (*Sov. J. Plasma Phys.* **10**, 605).

- P. S. Antsiferov, K. N. Koshelev, A. E. Kramida, and A. M. Panin (1989). *J. Phys. D* **22**, 1073.
- J. P. Apruzese and P. C. Kepple (1989). *AIP Conf. Proc.* **195**, 108.
- J. P. Apruzese and P. C. Kepple (1990). *J. Quant. Spectrosc. Radiat. Trans.* **44**, 529.
- L. E. Aranchuk, G. S. Bogolyubskii, G. S. Volkov, V. D. Korolev, Yu. V. Koba, V. I. Liksonov, A. A. Lukin, L. B. Nikandrov, O. V. Tel'kovskaya, M. V. Tupolov, A. S. Chernenko, Ya. V. Tsarfin, and V. V. Yankov (1986). *Fiz. Plazmy* **12**, 1324 (*Sov. J. Plasma Phys.* **12**, 765).
- J. Bailey, A. Fisher, and N. Rostoker (1986). *J. Appl. Phys.* **60**, 1939.
- V. I. Bayanov, V. A. Boiko, A. V. Vinogradov, S. S. Gulidov, A. A. Ilyukin, V. A. Katulin, A. A. Mak, V. Yu. Nosach, A. L. Petrov, G. V. Peregodov, S. A. Pikuz, I. Yu Skobelev, A. D. Starikov, A. Ya. Faenov, V. A. Chirikov, and E. A. Yukov (1976). *Pis'ma Zh. Eksp. Teor. Fiz.* **24**, 352 (*JETP Lett.* **24**, 319).
- R. Beier and H. -J. Kunze (1978). *Zeits. Phys. A* **285**, 347.
- W. H. Bennett (1934). *Phys. Rev.* **45**, 89.
- C. P. Bhalla, A. H. Gabriel, and L. P. Presnyakov (1975). *Mon. Not. R. Astron. Soc.* **172**, 359.
- D. Book, E. Ott, and M. Lampe (1976). *Phys. Fluids* **19**, 1982.
- S. I. Braginskii (1957). *Zh. Eksp. Teor. Fiz.* **33**, 645. (*Sov. Phys. JETP* **6**, 494).
- C. Breton, C. DeMichelis, and M. Mattiolo (1978). *JQRST* **19**, 367.
- R. Burhenn, B. S. Harn, S. Gossling, H. -J. Kunze, and D. Miclczarski (1984). *J. Phys. D* **17**, 1665.
- P. J. Burkhalter, J. Shiloh, A. Fisher, and R. D. Cowan (1979). *Appl. Phys.* **50**, 4532.
- P. G. Burkhalter, C. M. Dozier, and D. J. Nagel (1977). *Phys. Rev. A* **15**, 700.
- Yu. A. Bykovskii and V. V. Lagoda (1982). *Zh. Eksp. Teor. Fiz.* **56**, 114 (*Sov. Phys. JETP* **56**, 61).
- J. P. Chittenden (1989). *AIP Conf. Proc.* **195**, 118.
- J. P. Chittenden and M. G. Haines (1990). *Phys. Fluids B* **2**, 1889.
- P. Choi, A. E. Dangor, C. Deeney, H. Herold, and C. S. Wong (1987) "Experimental Investigation of Hotspot and Electron Beam Formation in a Gas Puff z-pinch and a Plasma Focus," presented at the IEEE International Conference on Plasma Science, Arlington, VA.
- S. S. Churilov, L. A. Dorokhin, K. N. Koshelev, and Yu. V. Sidelnikov, *JQSR T* **44**, 567 (1990).
- W. A. Cilliers, R. U. Datla, and H. R. Griem (1975). *Phys. Rev. A* **12**, 1408.
- F. L. Cochran and J. Davis (1990). *Phys. Fluids B* **2**, 1238.
- L. Cohen, U. Feldman, M. Swartz, and J. H. Underwood (1968). *J. Opt. Soc. Am.* **58**, 843.
- R. U. Datla and H. R. Griem (1978). *Phys. Fluids* **21**, 505.
- R. U. Datla and H. R. Griem (1979). *Phys. Fluids* **22**, 1415.
- G. Decker, W. Kies, M. Malzig, Yu. V. Sidelnikov, C. van Calker, G. Ziethon, H. Bluhin, D. Rusch, and W. Ratajczak (1990). *Nucl. Fusion* (in press).
- C. Deeney, T. Nash, P. D. LePell, K. Childers, and M. Krishnan (1989). *AIP Conf. Proc.* **195**, 62.
- H. M. Epstein, W. J. Callagher, P. J. Mallozzi, and T. F. Stratton (1970). *Phys. Rev. A* **2**, 146.
- F. S. Felber (1982). *Phys. Fluids* **25**, 643.
- N. V. Fillipov (1983). *Fiz. Plazmy* **9**, 25. (*Sov. J. Plasma Phys.* **9**, 14).
- M. Finkenthal, J. L. Schwob, and P. Mandelbaum (1986). *J. de Physique* **47**, C6-129.
- J. Fukai and E. J. Clothiaux (1975). *Phys. Rev. Lett.* **34**, 863.
- A. H. Gabriel and C. Jordan (1972a). *Case Studies in Atomic Collision Physics*, edited by McDaniel and McDowell (Amsterdam, North-Holland, 1972, v. 2., p. 209).
- A. H. Gabriel (1972b). *Mon. Not. R. Astron. Soc.* **160**, 99.
- M. Gersten, W. Clark, J. Rauch, G. M. Wilkinson, J. Katzenstein, R. D. Richardson, J. Davis, D. Duston, J. P. Apruzese, and R. Clark (1986). *Phys. Rev. A* **33**, 477.
- J. L. Giuliani (1989). *AIP Conf. Proc.* **195**, 124.
- E. Ya. Gol'ts, I. A. Zhitnik, E. Ya. Kononov, S. L. Mandelshtam, and Yu. V. Sidelnikov (1975). *Dok. Akad. Nauk SSSR* **220**, 560 (*Sov. Phys. Dokl.* **20**, 49).
- E. Ya. Gol'ts, G. V. Koloshnikov, K. N. Koshelev, A. E. Kramida, Yu. V. Sidelnikov, V. V. Vikhrev, V. V. Ivanov, A. A. Palkin, and V. V. Prut (1986). *Phys. Lett. A* **115**, 114.
- E. Ya. Gol'ts, L. A. Dorokhin, K. N. Koshelev, A. E. Kramida, A. A. Palkin, and Yu. V. Sidelnikov (1987). *Phys. Lett. A* **119**, 359.
- M. G. Haines (1960). *Proc. R. Soc. London* **76**, 250.
- J. E. Hammel (1976). "The Joule heating of a stable pinched plasma," LANL Report LA-6023-MS.
- B. A. Hammel and L. A. Jones (1984). *Appl. Phys. Lett.* **44**, 667.
- J. D. Hares, R. E. Marrs, and R. J. Fortner (1985). *J. Phys. D* **18**, 627.
- T. Holstein (1951). *Phys. Rev.* **83**, 1159.
- R. H. Huddlestone and S. L. Leonard (1965). *Plasma Diagnostic Techniques* (Academic, New York).
- G. V. Ivanenkov, A. N. Lebedev, S. A. Pikuz (1989). "Spectral investigations of a z-pinch," Preprint No. 210, P. N. Lebedev Institute, Moscow.
- V. V. Ivanov (1986). Dissertation, Kurchatov Institute, Moscow.
- V. L. Jacobs, J. Davis, P. C. Kepple, and M. Blaha (1977). *Astrophys. J.* **211**, 605.
- M. Klapisch, J. L. Schwob, B. S. Frankel, and J. Ored (1977). *J. Opt. Soc. Am.* **67**, 148.
- D. R. Kania and L. A. Jones (1984). *Phys. Rev. Lett.* **53**, 166.
- G. V. Koloshnikov, K. N. Koshelev, Yu. V. Sidelnikov, and S. S. Churilov (1985). *Fiz. Plazmy* **11**, 259 (*Sov. J. Plasma Phys.* **11**, 150).
- E. Ya. Kononov, K. N. Koshelev, and Yu. V. Sidelnikov (1977). *Fiz. Plazmy* **3**, 663 (*Sov. J. Plasma Phys.* **3**, 375).
- E. Y. Kononov, K. N. Koshelev, V. I. Safronova, Yu. V. Sidelnikov, and S. S. Churilov (1980). *Pis'ma Zh. Eksp. Teor. Fiz.* **31**, 720 (*JETP Lett.* **31**, 679).
- E. Ya. Kononov (1983). *Physica Scripta* **27**, 117.
- E. Ya. Kononov, K. N. Koshelev, and Yu. V. Sidelnikov (1985). *Fiz. Plazmy* **11**, 927 (*Sov. J. Plasma Phys.* **11**, 538).
- E. D. Korop, B. E. Meierovich, Yu. V. Sidelnikov, and S. T. Sukhorukov (1979). *Usp. Fiz., Nauk* **129**, 87 (*Sov. Phys. Usp.* **22**, 727).
- K. N. Koshelev, Y. V. Sidelnikov, and V. V. Vikhrev (1985). *Nucl. Instrum. Methods B* **9**, 704.
- K. N. Koshelev, V. I. Krauz, N. G. Reshetniak, R. G. Salukvadze, Yu. V. Sidelnikov, and E. Ya. Khahtiev (1988). *J. Phys. D* **21**, 1827.
- T. N. Lee and R. C. Elton (1971). *Phys. Rev. A* **3**, 865.
- T. N. Lee (1974). *Astrophys. J.* **190**, 467.
- T. N. Lee (1975). *Ann. N.Y. Acad. Sci.* **251**, 112.
- I. R. Lindemuth (1990). *Phys. Rev. Lett.* **65**, 179.
- B. E. Meierovich (1984). *Phys. Rep.* **104**, 259.
- B. E. Meierovich (1985). *Fiz. Plazmy* **11**, 1446 (*Sov. J. Plasma Phys.* **11**, 831).
- B. E. Meierovich (1986). *Usp. Fiz. Nauk* **149**, 221 (*Sov. Phys. Usp.* **29**, 506).
- R. A. Millikan and R. A. Sawyer (1918). *Phys. Rev.* **12**, 167.
- S. Morita and J. Fujita (1983). *Appl. Phys. Lett.* **43**, 443.
- C. R. Negus and N. J. Peacock (1979). *J. Phys. D* **12**, 91.
- A. N. Oraevskii, O. G. Semenov, and B. N. Chichkov (1987). *Kvan. Elektron* **14**, 1998 [*Sov. J. Quant. Electr.* **17**, 1274].
- N. J. Peacock (1968). Private communication.
- N. J. Peacock, R. J. Speer, and M. G. Hobby (1969). *J. Phys. B* **2**, 798.
- R. S. Pease (1957). *Proc. R. Soc. B* **70**, 445.
- N. R. Pereira and K. G. Whitney (1988a). *Phys. Rev. A* **38**, 319.
- N. R. Pereira and J. Davis (1988b). *J. Appl. Phys.* **64**, R1.
- N. R. Pereira (1990). *Phys. Fluids B* **2**, 677.
- D. E. Post, R. V. Jensen, C. B. Tarter, W. H. Grasberger, and W. A. Lokke (1977). *At. Data. Nucl. Data Tables* **20**, 397.
- J. C. Riordan, J. S. Pearlman, M. Gersten, and J. E. Rauch, "Sub-kilovolt x-ray emission from imploding wire plasmas," in *AIP Conference Proceedings*, Vol. 75, edited by D. Attwood and B. Henke.
- A. E. Robson (1989a). *Phys. Fluids B* **1**, 1834.
- A. E. Robson (1989b). *Phys. Rev. Lett.* **63**, 2816.
- A. Schultz, R. Burhenn, F. B. Rosmej, and H. J. Kunze (1989). *J. Phys. D* **22**, 659.
- J. J. Schwob and B. S. Frankel (1972). *Phys. Lett.* **40A**, 81.
- J. F. Seely and T. N. Lee (1984). *Phys. Rev. A* **29**, 411.
- J. W. Shearer (1976). *Phys. Fluids* **19**, 1426.
- Yu. V. Sidelnikov (1982a). Dissertation, Institute of Spectroscopy, USSR Academy of Sciences, Troitsk.
- Yu. V. Sidelnikov (1982b). *Zh. Tekh. Fiz.* **52**, 2283. (*Sov. Phys. Tech. Phys.* **27**, 1402).
- Yu. V. Sopkin, L. A. Dorokhin, K. N. Koshelev, and Yu. V. Sidelnikov (1991). *Phys. Lett. A* (submitted).
- C. Stallings, K. Childers, I. Roth, and R. Schneider (1979). *Appl. Phys. Lett.* **35**, 524.

- R. E. Stewart, D. D. Dietrich, P. O. Egan, R. J. Fortner, and R. J. Dukart (1987). *J. Appl. Phys.* **61**, 126.
- B. A. Trubnikov and S. K. Zhdanov (1976). *Zh. Eksp. Teor. Fiz.* **70**, 92. (*Sov. Phys. JETP* **43**, 48).
- J. J. Turecek and H. J. Kunze (1975). *Zeits. Phys. A* **273**, 111.
- L. A. Vainshtein and U. I. Safronova (1978). *Atomic Data and Nuclear Data Tables* **21**, 49.
- L. A. Vainshtein, I. I. Sobelman, and E. A. Yukov (1979). *Excitation of Atoms and Broadening of Spectral Lines*, Nauka, Moscow; also Springer Verlag, Berlin and New York (1981).
- V. A. Veretennikov, V. A. Gribkov, E. Ya. Kononov, O. G. Semenov, and Yu. V. Sidelnikov (1981a). *Fiz. Plazmy* **7**, 455. (*Sov. J. Plasma Phys.* **7**, 249).
- V. A. Veretennikov, S. N. Polukhin, O. G. Semenov, and Yu. V. Sidelnikov (1981b). *Fiz. Plazmy* **7**, 1199. (*Sov. J. Plasma Phys.* **7**, 656).
- V. A. Veretennikov, A. N. Dolgov, A. I. Isakov, V. L. Kontsyrev, O. N. Krokhin, A. P. Nekunde, O. V. Sagalovskaya, O. G. Semenov, Yu. V. Sidelnikov, V. V. Ulyanov (1982). *Pisma Zh. Eksp. Teor. Fiz.* **8**, 1041 (*Sov. Tech. Phys. Lett.* **8**, 448).
- V. A. Veretennikov, A. N. Dolgov, O. N. Krokhin, and O. G. Semenov (1985). *Fiz. Plazmy* **11**, 1007. (*Sov. J. Plasma Phys.* **11**, 587).
- V. V. Vikhrev (1977). *Fiz. Plazmy* **3**, 98 (*Sov. J. Plasma Phys.* **3**, 539).
- V. V. Vikhrev (1978a). *Pis'ma Zh. Eksp. Teor. Fiz.* **27**, 104 (*JETP Lett.* **27**, 95).
- V. V. Vikhrev and K. G. Gureev (1978b). *Zh. Tekh. Fiz.* **48**, 2264. (*Sov. Phys. - Tech. Phys.* **23**, 1295).
- V. V. Vikhrev, V. V. Ivanov, and K. N. Koshelev (1982a). *Fiz. Plazmy* **8**, 1211. (*Sov. J. Plasma Phys.* **8**, 688).
- V. V. Vikhrev, V. V. Ivanov, K. N. Koshelev, and Yu. V. Sidelnikov (1982b). *Dokl. Akad. Nauk SSSR* **262**, 1361 (*Sov. Phys. Dokl.* **27**, 153).
- A. V. Vinogradov, I. Yu. Skobelev, and E. A. Yukov (1977). *Zh. Eksp. Teor. Fiz.* **72**, 1762. (*Sov. Phys. JETP* **45**, 925).
- I. V. Volobuev, V. A. Gribkov, D. Denuš, N. V. Kalachev, T. A. Kozlove, O. N. Krokhin, S. Sledzinski, S. A. Startsev, and S. Czekaj (1988). *Fiz. Plazmy* **14**, 682. (*Sov. J. Plasma Phys.* **14**, 401).
- T. J. Welch and E. J. Clothiaux (1974). *J. Appl. Phys.* **45**, 3825.
- F. Winterberg (1978). *Zeits. Phys. Z* **284**, 43.
- F. C. Young, S. J. Stephanakis, and D. Mosher (1977). *J. Appl. Phys.* **48**, 3642.
- S. M. Zakharov, G. V. Ivanenkov, A. A. Kolomenskii, S. A. Pikuz, and A. I. Samokhin (1983). *Fiz. Plazmy* **9**, 469. (*Sov. J. Plasma Phys.* **9**, 271).